Journal of Materials Research and Technology 38 (2025) 5780–5796

Contents lists available at ScienceDirect

Journal of Materials Research and Technology

journal homepage: www.elsevier.com/locate/jmrt

Development of a semi-empirical approach correlating ion- and neutron-induced hardening in Eurofer97 using nanoindentation and crystal plasticity finite element method

Tymofii Khvan [a], Ludovic Noels [b], Dmitry Terentyev [c], Enrico Corniani [d,*], Peter Hähner [d], Chih-Cheng Chang [c,e]

[a] NOMATEN Centre of Excellence, National Center for Nuclear Research, Andrzeja Sołtana 7, Otwock, 05-400, Poland
[b] Aerospace and Mechanical Engineering Department, University of Liège, Allée de la Découverte 9, Liège, 4000, Belgium
[c] Institute for Nuclear Materials Science, SCK-CEN, Boeretang 200, Mol, 2400, Belgium
[d] European Commission, Joint Research Centre, Westerduinweg 3, Petten, 1755 LE, The Netherlands
[e] Université Catholique de Louvain, Place de l'Université 1, Ottignies-Louvain-la-Neuve, 1348, Belgium

ARTICLE INFO

Keywords:
Nanoindentation
Ion irradiation
Finite element method
Crystal plasticity
Irradiation hardening

ABSTRACT

An experimentally-based computational methodology is developed to predict the irradiation hardening in materials for nuclear applications, aimed at avoiding neutron irradiation. The results are expected to accelerate the delivery of new research data in nuclear materials science by reducing the time, costs, and resources necessary for neutron irradiation. The effect of ion irradiation on nanohardness is measured with nanoindentation and computationally replicated on the basis of the tensile tests data from neutron-irradiated specimens. Thus, the established procedure aims to interconnect two important phenomena: the effect of ion vs. neutron irradiations on mechanical properties; and the nanocompressive vs. macrotensile deformation. The accuracy of the outcoming results is discussed. The tests performed are used to establish and validate a crystal plasticity finite element method model of irradiated Eurofer97 steel. The constitutive material law is modified with respect to the hardening caused by the neutron irradiation dose and is used to feed the crystal plasticity finite element method model of the nanoindentation process. This consequently allows one to accurately reproduce the experimental hardness–depth values obtained from the ion-irradiated specimen. Eventually, a basic proof of concept is provided, which can be further refined for the prediction of neutron-induced hardening, while working only with ion-irradiated material.

1. Introduction

The development of innovative nuclear reactors requires a comprehensive knowledge about the mechanical properties and the environmental performance of the structural materials chosen for the construction of their components. Conventional mechanical testing can be applied to deduce these properties under variable conditions, such as temperature or strain rate. An effective design of nuclear components additionally relies on the behavior of the materials under constant neutron irradiation. Structural components suffer from radiation-induced degradation [1–6], imposing strong limitations on the development of new materials for nuclear applications. Moreover, neutron irradiation leads to activation, hence its use in the research context requires significant time, costs, and human resources. The development of reliable experimental techniques aimed at effectively determining the radiation-induced degradation (e.g., irradiation hardening) of the mechanical properties is an essential objective of nuclear materials research. These techniques must reduce the resources needed for irradiation or post-irradiation examination.

A partial solution to reduce the activity levels is to rely on the miniaturization concept [7–9] by reducing the dimensions of samples. However, another problem is the level of displacement damage achievable. For instance, current Gen II fission reactors may achieve up to 50 dpa damage for in-vessel components, while future Gen IV designs may exceed 150 dpa [10,11]. Such magnitudes of damage doses are extremely high for any materials test reactor to be achieved in a reasonable time, hence limiting the availability of test results. Today, test reactors are capable of providing 3–5 dpa/year, commercial fast-neutron reactors up to 20 dpa/year [12,13], the use of which, however, is limited for research purposes.

* Corresponding author.
E-mail address: enrico.corniani@ec.europa.eu (E. Corniani).

https://doi.org/10.1016/j.jmrt.2025.08.235
Received 28 July 2025; Accepted 26 August 2025
Available online 2 September 2025

Therefore, the nuclear materials scientific community is increasingly exploring ion irradiation to emulate neutron irradiation damage. Irradiation with heavy ions is virtually unlimited in terms of damage scales, as the magnitudes can reach tens of dpa in hours. It is 100 to 1000 times cheaper than neutron irradiation [12], as it requires a particle accelerator instead of a complete nuclear fuel-powered fission reactor. Using heavy ions for irradiation typically leaves negligible residual activity, allowing the samples to be tested soon after exposure without extra safety measures. Ion irradiation is generally safe, cost-effective, and fast, but it has distinct limitations due to the differences in how neutrons and ions interact with matter. Neutrons, being uncharged, cause a broad range of energy transfers during nuclear collisions, producing a wide distribution of primary knock-on atoms (PKAs). Conversely, heavy ions, as charged particles, interact through Coulomb forces, leading to more localized energy transfer and a narrower PKA spectrum. Consequently, neutron-induced damage is more evenly spread throughout the material, whereas heavy ion damage is confined to a thin surface layer, typically a few micrometers deep, varying with ion energy and material type [14–20].

To accurately assess the effects of ion damage, nano- or microscale characterization techniques, such as nanoindentation (NI) [21], that can provide standardized mechanical property measurements must be employed. It can be additionally supported by microstructural investigations using scanning or transmission electron microscopy (S/TEM), and atomic force microscopy (AFM). The substantial difference between neutron and heavy ion irradiations relates to neutron-induced transmutation and gas production (hydrogen or helium leading to bubbles and embrittlement) in the target material [16,19,22]. Heavy ions, while capable of causing atomic displacements, do not induce significant transmutation; conversely, they deposit a higher amount of interstitial nuclei in the crystal lattice of the target material and facilitate ion beam mixing [19]. Factors like the choice of ion species, energy and irradiation temperature need careful consideration to mimic specific aspects of neutron damage [14,15,18,19]. Moreover, it is known that the difference in irradiation dose rates may lead to different degrees of irradiation hardening in FeCr-based materials [23]. Therefore, the effect of the dose rate must be accounted as well to ensure the transferability of the ion and neutron damage. Recently, there was a proposal to use a temperature shift (to raise up irradiation temperature of ions) to compensate for the higher dose rate (3–4 orders of magnitude compared to neutrons) [24]. However, the irradiation investigations from this work were performed in the frame of a larger project [25] where the irradiation conditions for ions were decided for a group of materials. It has been decided to execute the irradiation at equivalent temperatures and compare the mechanical response.

Research mostly relies on simulations software like SRIM (Stopping and Range of Ions in Matter) [26] to estimate damage profiles and guide experimental design; it has been shown that different software applications may disagree quite substantially on the simulated damage profile [27]. The use of NI in nuclear materials science is rapidly emerging nowadays, as it is able to characterize the properties of the material using a minimum testing volume, which complies with the mentioned miniaturization concept, while the characteristic depth lies within the range of hundreds nanometers to tens micrometers, which makes NI a tool of choice to study the impact of ion irradiation and its relation with neutron irradiation damage.

In combination with computational analysis using the finite element method (FEM), NI can expand the understanding of the physical processes occurring during the deformation. With a proper experimental validation, this combination can provide underpinning knowledge about fundamental quantities associated with the deformation process (stress, strain, dislocation density, etc.). As in the works of P. Lin et al. [28–31] or X. Xiao et al. [32–34] FEM simulations of the NI process in irradiated materials for nuclear applications are commonly applied. More general applications of microscopy or modeling techniques to support NI testing for nuclear materials, including ion-irradiated materials, are provided in Refs. [35–40]. Briefly, the mentioned works aim at predicting the plastic properties from tests done below the ductile-to-brittle transition temperature, after irradiation hardening, studying grain boundary effects, etc. Furthermore, S/TEM or AFM is generally applied to support the experimental process and reconfirm the measured data. In [41], for example, TEM was used to analyze the evolution of the subsurface microstructure due to irradiation, where the depth of the hardening peaks was found to be in good correlation with the highest concentration of irradiation defects. In [42] a systematic study of the heights of indentation pile-ups is performed using AFM, providing their dependence on the microstructural state of the indented specimen. A good overview of recent challenges and solutions in nanoindentation testing and modeling of ion-irradiated materials can be found with [43].

In this work, a novel semi-empirical approach to characterize and interconnect the macro- and microscale plastic behavior of irradiated materials for nuclear applications is introduced. Crystal plasticity finite element method (CPFEM) modeling is supported by experimental characterization to reproduce mechanical responses affected by ion and neutron irradiations. The proposed research aims to develop a methodology that allows one to evaluate radiation-induced hardening in a neutron-irradiated material using NI tests applied to an ion-irradiated material. This effect is assumed to be comparable for materials exposed to both types of irradiation at the same dose and similar irradiation temperatures. CPFEM modeling allows the simulation of the NI process of a specimen with a modified subsurface, mimicking the effect of ion irradiation. In addition, NI tests can be used to validate those modifications. Eventually, the correctly obtained (experimentally validated) hardening–dose function introduced to the subsurface layer of the NI model may be used as a modification representing the effect of irradiation. Thus, a predictive tool is established that allows the characterization of the irradiated material in a cost-effective and convenient way (i.e., without radiation-induced activation) and to use these data to computationally model its macroscale behavior under operational conditions and desired geometry.

The approach is validated by NI and tensile tests applied to reduced activation ferritic/martensitic (RAFM) steel Eurofer97, a well-studied material [44,45] developed for structural components in future fusion and Gen IV reactors [46–48]. This material plays a crucial role for in-vessel components. Many studies are oriented towards the development of modified chemical compositions and subsequent thermomechanical treatments, thus providing new materials with better properties; however, still based on the reference examples (Eurofer97, T91, F82H, etc.) [49–53]. Any new product would benefit from relatively simple and fast methods to estimate their properties after irradiation and radiation tolerance. Eurofer97 is a reference material for the development of new methods, aimed at a faster, safer and cheaper characterization of materials for nuclear applications.

2. Methodology

2.1. Simulations of the ion damage

The idea that prompted this work was to find an efficient representation of the ion-irradiated subsurface, which will be sensitive to the non-uniform distribution of damage. Therefore, NI simulations of the ion-irradiated material are performed by division of the ion-irradiated subsurface into distinct layers (four in the case of this work) to comply with variable damage levels; see Fig. 1. Furthermore, the layer input parameters must be related to conventional mechanical properties in order to simplify the connection with the effect of neutron irradiation (i.e., limited post-irradiation testing capabilities). Hardness is known to be closely related to the yield stress [54–56], the standard property measured in metallic materials, including neutron-irradiated. Thus, each layer is assigned to a reference constitutive law, however modified to account for the effect of irradiation hardening (increased

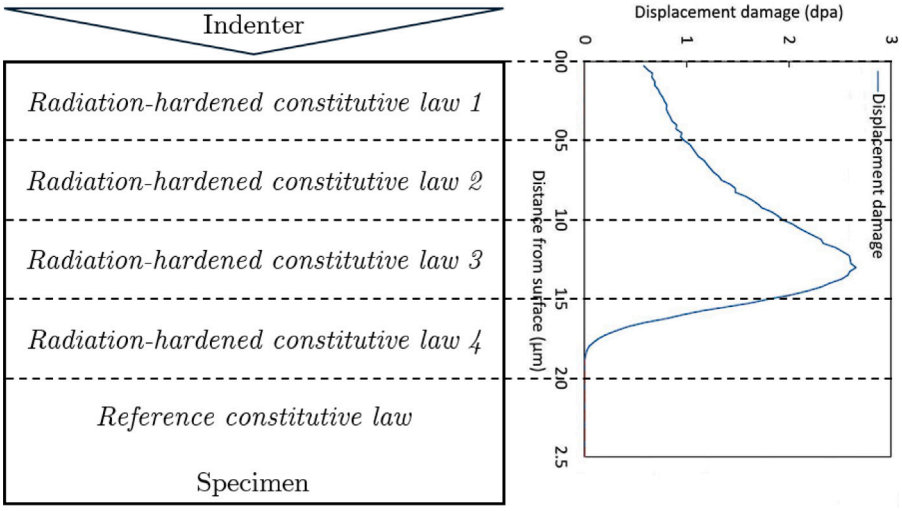

Fig. 1. Schematic representation of the layered geometry.

yield stress) typical of an average damage dose expressed in dpa in that region (i.e., layer).

The concept is to find simulation parameters that provide the constitutive laws with yield stress values that (a) follow the distribution of the damage dose according to the damage-depth profile; (b) are appropriate for the replication of the NI hardness–depth profiles obtained experimentally. The idea is shown schematically in Fig. 1. It is assumed that the constitutive laws obtained will be representative for the neutron-irradiated material and can be used to simulate large-scale tests and complex geometries through FEM. The irradiation parameters, however, must be carefully selected to ensure similar damage accumulation.

Eventually, an ion-irradiated specimen can be used for the characterization of radiation-induced hardening of a material in a range of doses, the selection of which is dependent on the ion-irradiation parameters. The selection of the number of layers to be four is originally assumptive, aimed at a sufficient replication of the SRIM profile, while keeping a low demand for the calculation and fitting time. Nevertheless, increasing the number of layers to eight did not show any significant improvement in the result.

The present work first establishes and demonstrates the reverse procedure: knowledge of the impact of neutron damage allows reproducing the behavior of an ion-irradiated material. The constitutive laws are modified with respect to the tensile tests data for the neutron-irradiated material available in the literature [57], and then used as layer inputs in the simulations of the NI process. Eventually, once the NI simulations with the modified subsurface reproduce their experimental ion-irradiated analogues, a proof-of-concept is obtained, allowing the use of tensile test data after neutron irradiation to simulate NI tests after ion irradiation. Obviously, when NI analysis of ion-irradiated materials is discussed, the real interest and ultimate goal is to use it to predict the effect of neutron damage. The reverse approach allows one to confirm the validity of the idea, while it is of no practical application (it is worthless to irradiate a material with neutrons to predict ion irradiation damage). As the second step, the sought algorithm is implemented, in which results obtained by manual fitting are presented providing decent accuracy. The correct approach is crucial to make this method useful in real applications. Both approaches are compared in Fig. 2.

While the method can still be used by applying the manual fitting, it remains an inaccurate and time-consuming procedure. The development of a computational algorithm assigned to the fitting of the complex hardening–depth–dose function can be proposed. It is based on iterative NI simulations of ion-irradiated material, which are crucial for the evaluation of the constitutive parameters responsible for the irradiation hardening and, therefore, macroscale simulations of the material emulating the effect of neutron irradiation.

The algorithm that combines all aspects of the proposed method is illustrated in Fig. 3.

2.2. Description of the CPFEM framework

The computational analysis has been done by coupling a user-defined material law (UMAT subroutine) that implements crystal plasticity theory to a FEM solver. The solver is combined with the open source three-dimensional finite element mesh generator with a built-in CAD engine: gmsh [58]. The CM3 libraries FEM solver [59] was developed in the Department of Aerospace and Mechanical Engineering of the University of Liege in Belgium, while the crystal plasticity routine was developed by Delannay et al. [60,61]. Here a short review of the constitutive formulations and the introduction of the irradiation effect will be given, while Ref. [62] provides a detailed description of the applied crystal plasticity framework.

2.2.1. Modeling of plastic deformation

Elasticity is determined through the elastic coefficients C_{11}, C_{12}, and C_{44}, which are enough to establish the stiffness tensor in a BCC material, due to the symmetry of cubic crystals. Plasticity is assumed to be caused only by the glide of dislocations, as the main mechanism relevant to structural materials. The strain rate is then controlled by the rate at which dislocations are released from pinning points, which is thermally activated and driven by the applied stress. Thermal activation and obstacles overcome by dislocations are predicted by an Arrhenius-type equation [63,64]. The dislocation slip rate $\dot{\gamma}^{\alpha}$ in a slip system α may be expressed as a function of the shear stress τ_{α} in this slip system [65]:

$$\dot{\gamma}^{\alpha} = \dot{\gamma}_0 \exp\left(-\frac{G_0 \mu b^3}{k_B T}\right) 2\sinh\left[\frac{G_0 \mu b^3}{k_B T}\left(1-\left(1-\left(\frac{\tau_{\alpha}-\tau_c}{\hat{\tau}}\right)^{p}\right)^{q}\right)\right] \quad (1)$$

In this expression, $G_0 \mu b^3 = 2H_k$ represents the value of the enthalpy of kink-pair formation for a screw dislocation, where $\mu = (C_{11} - C_{12} + 2C_{44})/4$ is the shear modulus, b is the magnitude of the Burgers vector and G_0 is a constant. $\dot{\gamma}_0$ is a reference slip rate, $k_B T$ is the product of the Boltzmann constant and temperature, and p and q are constants that describe the profile of the Peierls potential barrier, being equal to 0.5 and 1.5 respectively [66]. The critical resolved shear stress (CRSS) is controlled by two terms: the athermal stress τ_c typical of BCC metals and the thermal stress $\hat{\tau}$, which determines the thermal sensitivity of the plastic flow.

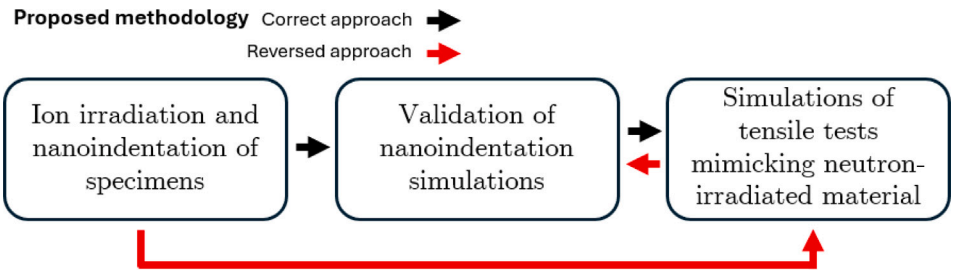

Fig. 2. Schematic comparison of the proposed methodology done in the correct and reverse way.

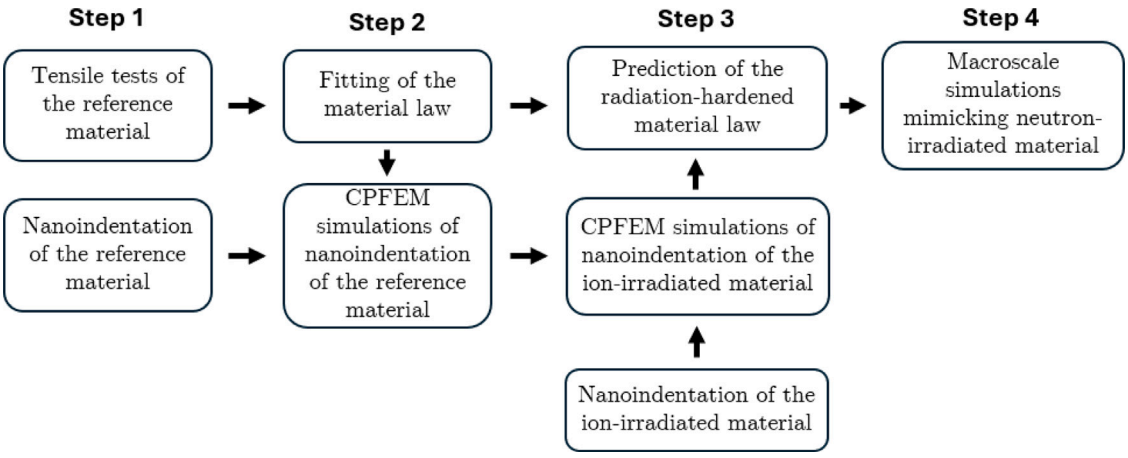

Fig. 3. The algorithm to evaluate the neutron-induced irradiation hardening.

Athermal stress can be expressed as a function of dislocation density ρ. To account for the effect of irradiation hardening, we introduce a hardening term S_{irr}:

$$\tau_{\mathrm{c}} = S_0 + S_{\mathrm{irr}} + h_{\mathrm{dis}}\mu b\sqrt{\rho} \tag{2}$$

where h_{dis} is the dislocation strength coefficient and S_0 represents the sum of the contributions of the lattice friction stress, the Hall–Petch effect [67], and other typical hardening mechanisms for steels, such as solid solution or precipitation hardening. S_{irr} depends on the introduced irradiation dose in dpa. Although this is the athermal contribution to the CRSS, it is known that h_{dis} in BCC metals may depend on temperature [68]. ρ is the dislocation density which evolves according to the modified law proposed by Kocks and Mecking [69]:

$$\dot{\rho} = (k_1\sqrt{\rho} - \xi k_2\rho)\dot{\Gamma} \tag{3}$$

Here k_1 is a fitting coefficient representing the rate of dislocations accumulation due to increase of plastic strain, and k_2 is a coefficient describing dislocation recovery rate due to their annihilation when having the opposite signs. k_2 is computed from the saturated dislocation density value ρ_{sat} and remains constant, and the temperature and strain rate effects are additionally controlled by the term ξ [70]:

$$\rho_{\mathrm{sat}} = \left(\frac{k_1}{\xi k_2}\right)^2 \tag{4}$$

$$\xi = \left\{1 - \left(\frac{k_{\mathrm{B}}T}{G_0}\ln\frac{\dot{\gamma}_0}{\dot{\Gamma}}\right)^{\frac{1}{q}}\right\}^{-\frac{1}{p}} \tag{5}$$

where $\dot{\Gamma}$ is the sum of the slip rates in all slip systems:

$$\dot{\Gamma} \triangleq \sum_{\alpha}|\dot{\gamma}_{\alpha}| \tag{6}$$

It is well known that strain softening due to annihilation of irradiation-induced defects may lead to plastic instability and deformation localization. The RAFM steel Eurofer97, however, represents a nano-structured material, the plastic deformation of which is dominated by high dislocation density and the martensite lath structure. The irradiation hardening term S_{irr} depending on dose only, decoupled from strain, what represents a reasonable simplification, while the strain dependence of the forest hardening by the dislocation density ρ is described by the Kocks–Mecking model in Eq. (3).

2.2.2. Stand-alone mode Taylor-type homogenization

The described crystal plasticity framework can be used either stand-alone or coupled with a finite element solver (CPFEM mode). In the stand-alone mode, the model equations are applied to a theoretical (virtual) polycrystal with one material point, in which every grain undergoes the same strain as the polycrystal as a whole (Taylor mean-field crystal plasticity model [71]). The grains of this virtual polycrystal are not defined in terms of their geometrical shape, size, and arrangement. Thus, the effect of these factors on the mechanical response is neglected. However, a specific crystallographic texture may be assigned to the polycrystal. Even though the iso-strain assumption makes the approach less realistic than CPFEM, the stand-alone calculations rely on the same mathematical modeling of dislocation slip and allow us to capture the main macroscopic trends.

In this work, the stand-alone mode is applied to replicate the constitutive laws of the material according to the uniaxial tensile tests, as their scale, geometric simplicity, and structural homogeneity are high enough. NI simulations are then performed using the CPFEM mode because they require a more complex geometrical setup and consideration of the crystal anisotropy effects.

2.3. Specimen preparation & experiments

The Eurofer97 material used in this work for all types of mechanical tests was produced by Böhler Edelstahl GmbH and commonly referred to as Batch 1. The heat was produced in the form of bars 100 mm in diameter. It was normalized at 980 °C for 1.5 h, and tempered at 740 °C

Table 1
Chemical composition of the Eurofer97 product in wt%.

Cr	C	Mn	V	W	Ta	N_2	O_2	P	S
8.87	0.12	0.42	0.19	1.1	0.14	0.018	0.0013	0.004	0.003
B	Ti	Nb	Mo	Ni	Cu	Al	Si	Co	As+Sn+Sb+Zr
<0.0005	0.008	<0.001	<0.001	<0.007	0.022	0.008	0.07	0.004	<0.015

Table 2
Surface preparation method of the Eurofer97 samples.

	Method	Parameters
Step 1	Mechanical grinding	500 grit grinding paper
Step 2	Mechanical grinding	1000 grit grinding paper
Step 3	Mechanical grinding	2000 grit grinding paper
Step 4	Mechanical polishing	3 μm diamond suspension
Step 5	Mechanical polishing	1 μm diamond suspension
Step 6	Active oxide polishing	OP-S (2 h)
Step 7	Electrolytic polishing	10% oxalic acid at 5 V

Table 3
Eurofer97 chemical composition and displacement energy (E_d) values chosen according to ASTM E521-16 recommendations.

Element	Composition wt%	E_d [eV]
Fe	90	40
Cr	8.9	40
W	1.1	90

Table 4
Testing parameters for the nanoindentation tests.

Parameter	Value
Loading type	Linear loading/force controlled
Max. load	20/100 mN
Loading/unloading time	30 s
Dwelling time	30 s
Acquisition rate	10 Hz

for 3.7 h, followed by air cooling. The chemical composition of the material is provided in Table 1, as reported by the manufacturer [72].

2.3.1. Polishing & ion irradiation of nanoindentation specimens

A set of Eurofer97 samples was cut with dimensions $10\times10\times1$ mm^3. One-sided grinding and mechanical polishing was used down to the active oxide polishing suspension "OP-S". As the final step, electrolytic polishing was applied at room temperature using 10% oxalic acid at a voltage of 5 V. The surface preparation steps are provided in Table 2.

One of the specimens was irradiated with iron ions at the Helmholtz-Zentrum Dresden-Rossendorf (HZDR) institute located in Dresden, Germany. The irradiation campaign was carried out as part of the M4F project [25]. Fe^{2+} ions of 5 MeV energy produced by the 3 MV Tandetron accelerator were used. The irradiation temperature was 300 °C. The total fluence was $2.4{\cdot}10^{15}$ ions/cm^2. Approximately 10 h were needed to reach 1 dpa, what gives the dose rate of $2.78{\cdot}10^{-5}$ dpa/s. Calculations using the binary collision code SRIM were performed to obtain the depth profiles of the displacement damage and the injected interstitial atoms. The calculations were based on the Kinchin-Pease model using the quick calculation mode with the lattice binding energy and the surface binding energy set to zero, as suggested by Stoller et al. [73]. The main chemical elements (elements above 1% in weight and rounded up to a closer value) of Eurofer97 together with their displacement energies recommended in the ASTM E521 standard [19] are provided in Table 3. The damage-depth profile is provided in Fig. 4. It shows an exponential increase in displacement damage from ~0.5 dpa on the surface to the Bragg peak of ~2.6 dpa at ~1.25 μm depth. Beyond this peak, damage decreases significantly, reaching zero at ~1.8 μm.

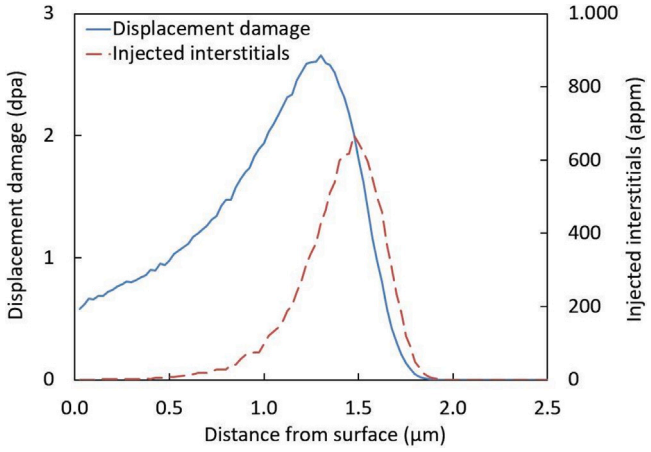

Fig. 4. Damage-depth profile for the ion-irradiated Eurofer97 specimen obtained with SRIM code.

2.3.2. Nanoindentation

Nanoindentation experiments were carried out in collaboration with the Micro-Characterization Laboratory of the Joint Research Centre of the European Commission in Petten, The Netherlands, within the Open Access program [74].

The equipment used in the indentation campaign was the Anton Paar UNHT^3 Ultra nanoindentation tester. The testing module consists of the indenter tip and a reference ball tip located at a distance of 9.3 mm from each other. The specimen is fixed by mechanical clamping. A picture of the testing module is provided in Fig. 5.

Nanoindentation single-cycle tests using a Berkovich tip were performed on Eurofer97 specimens in the reference (unirradiated) and ion-irradiated states. The ion damage-depth profile makes the material properties vary with depth; therefore, the tests were performed at two different loads of 20 mN and 100 mN corresponding to the penetrations of the tip to ~500 nm and ~1200 nm, respectively. The hardness and Young's modulus values were calculated using the Oliver-Pharr method [75]. The NI testing parameters are summarized in Table 4.

Fig. 6 shows that the measured elastic modulus of the material does not agree well with the commonly established value (~210 GPa) measured by other methods. Elevated unloading stiffness can originate from the formation of indentation pile-ups in the irradiation-hardened material; reduced stiffness from specimen compliance due to specimen fixation by mechanical clamping only. $10\times10\times1$ mm^3 size specimens appear to be insufficiently large to be properly fixed in the holder without gluing. To confirm the enhanced pile-up formation in the irradiated material, the 100 mN indents were inspected using a scanning electron microscope, as shown in Fig. 7.

In the Oliver-Pharr method, the unloading stiffness is the key quantity that is used to calculate both the contact area and the reduced modulus. Since hardness is most important to analyze the impact of the irradiation effect, a manual stiffness correction was performed. This was possible because the value of the elastic modulus of the material is known and changes only slightly with irradiation (in contrast to what is seen in Fig. 6). To apply the stiffness correction [76], the stiffness value is manually adjusted in the Oliver-Pharr equations to obtain the known value of Young's modulus of 210 GPa. This will consequently

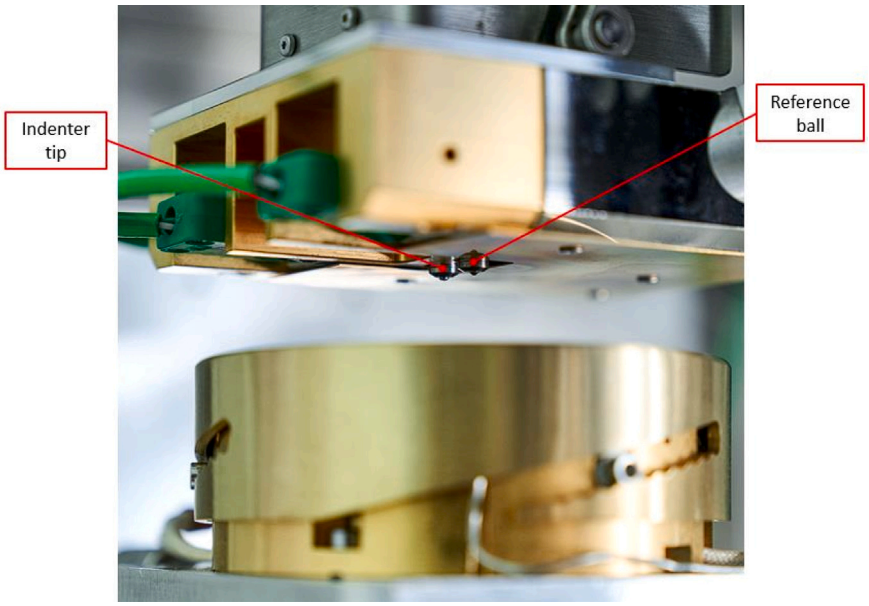

Fig. 5. Anton Paar UNHT^3 testing module. Copyright European Commission 2021.

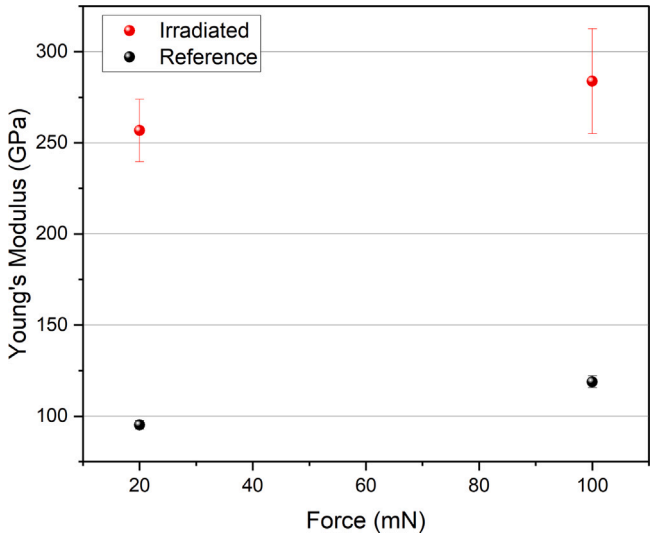

Fig. 6. Young's modulus versus indentation force.

correct the contact area affecting the hardness. A corrected contact area is used to determine a new corrected hardness. After applying this correction procedure, the hardness values were obtained as presented in Fig. 8. Here, the irradiation hardening effect is clearly seen: ~0.77 GPa hardness increase for 20 mN (~500 nm indentation depth) and ~0.42 GPa for 100 mN force (~1200 nm indentation depth). One also notes that the magnitude of the irradiation hardening decreases with depth. This is expected because at larger depths the effect of the irradiated zone diminishes as more non-irradiated material is involved in the deformation process.

2.3.3. Tensile tests of unirradiated material

Tensile tests were carried out on non-irradiated miniaturized flat tensile samples (dogbone) with a gauge length of 5.2 mm and a cross-sectional area of 1×1.6 mm^2 using an INSTRON model 1362 coupled with a load cell of 100 kN. To correctly estimate the $\hat{\tau}$ parameter from Eq. (1) controlling the thermal sensitivity of the plastic flow, two different test temperatures were required. Therefore, tests were carried out at room temperature and 300 °C at a strain rate of $2.78 \cdot 10^{-4}$ s^{-1}. Tensile properties were established according to the ASTM E8/E8M [77] standard. The engineering stress–strain curves and the corresponding recalculated true stress–strain curves are presented in Fig. 9. A classical thermally-activated behavior can be seen, where the yield stress, hardening rate, and uniform elongation decrease with respect to temperature.

3. CPFEM analysis of Eurofer97 in the reference and irradiated state

In this section, the described methodology and experimental data from Section 2 are applied to interconnect the material behavior after neutron and ion irradiation. To this end, data from the tensile tests performed on the unirradiated material (Section 2.3.3) are replicated using the computational framework described in Section 2.2, and then modified to correspond to the yield stresses of the neutron-irradiated material available in the literature [57]. These data are used as input for the CPFEM simulations of the nanoindentation process into the specimen box with the layered subsurface, as described in Section 2.1 and shown in Fig. 1. The simulation results obtained are then compared with the experiments and the FEM maps of the distributions of stress, accumulated slip, and dislocation densities are analyzed and discussed.

3.1. Adoption of the constitutive laws

To establish the elastoplastic behavior of the material, a set of parameters responsible for the formation of the dislocation slip described in Section 2.2 has to be determined. The number of active slip systems was taken as 24, the elastic constants C_{11}, C_{12}, and C_{44} were taken from [78], the Burgers vector was taken for the $\frac{a}{2}\langle 111\rangle$ dislocation (so the magnitude of the Burgers vector is $\frac{\sqrt{3}}{2}a$), where a is α-Fe lattice parameter of 2.856 Å [79], and $2H_k$ was determined in Ref. [80]. This value was adopted in this work to reflect the presence of carbon impurities, which interact with the kinks, effectively increasing the apparent activation energy. Atomistic simulations describing such an interaction can be found in Ref. [81]. The initial dislocation density is widely available in the literature for Eurofer97 [51,82], and is commonly measured to be around 10^{14} m^{-2}. Here the value of $5.5 \cdot 10^{13}$ m^{-2} is taken because it gave a better fit to the simulated curves. This reduction can be attributed to a smaller fraction of mobile dislocations

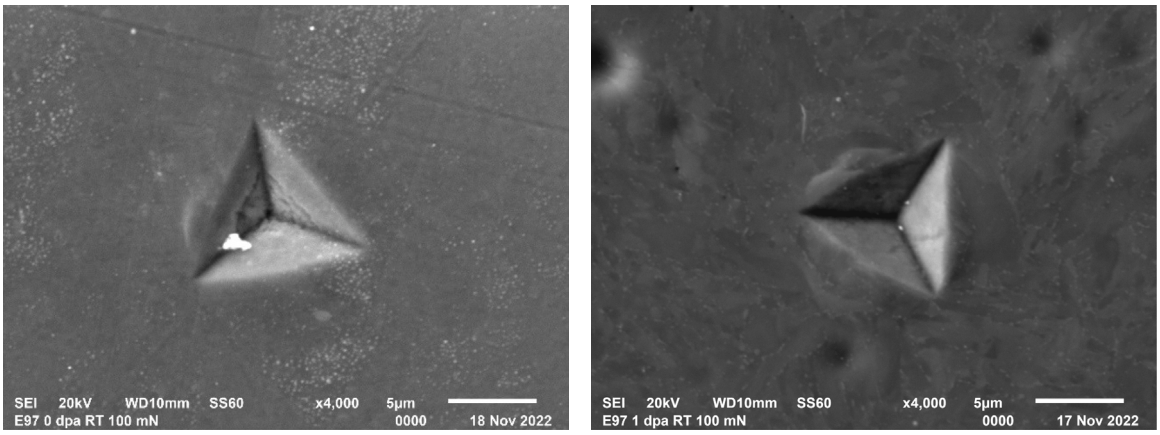

(a) Non-irradiated. (b) Ion-irradiated.

Fig. 7. 100 mN indents placed on Eurofer97: (a) non-irradiated; (b) ion-irradiated.

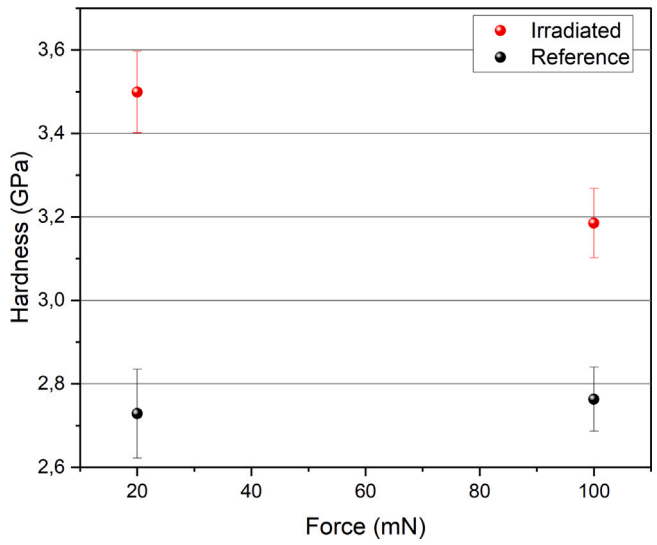

Fig. 8. Corrected nanoindentation hardness values versus indentation force.

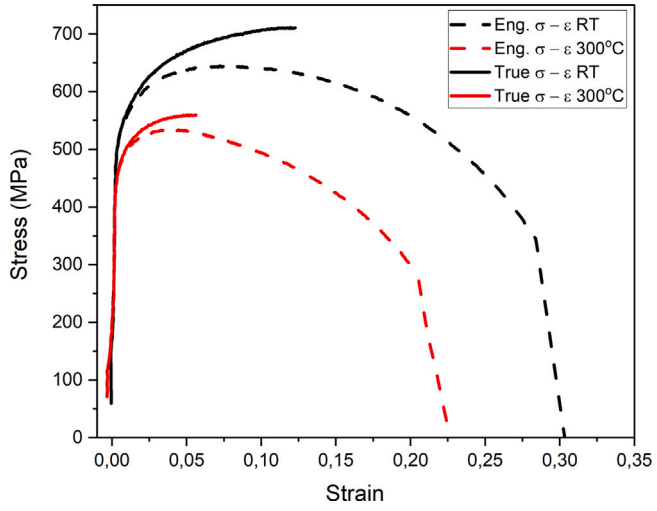

Fig. 9. Engineering and true stress–strain curves for Eurofer97 at two different temperatures.

Table 5
List of constitutive parameters used to simulate the material law of the unirradiated Eurofer97. For some parameters, more than one value can reproduce the transition from room temperature to 300 °C.

Parameter	Value	Source
Elastic coefficient, C_{11}	230 [GPa]	Ref. [78]
Elastic coefficient, C_{12}	135 [GPa]	Ref. [78]
Elastic coefficient, C_{44}	117 [GPa]	Ref. [78]
Burgers vector length, b	0.2482 [nm]	Ref. [79]
Shear modulus, μ	82.25 [GPa]	Calculated
Reference slip rate, $\dot{\gamma}_0$	10 [s^{-1}]	Fitted
Strengthening mechanisms, S_0	100 [MPa]	Fitted
Initial dislocation density, ρ_0	$5.5{\cdot}10^{13}$ [m^{-2}]	Ref. [82]/decreased
Kink pair formation enthalpy, $2H_k$	2.365 [eV]	Ref. [80]/increased [81]
Dislocation interaction strength, h_{dis}	0.13–0.115 [–]	Fitted
Saturated dislocation density, ρ_{sat}	$2.75{\cdot}10^{15}$ [m^{-2}]	Fitted
Kocks–Mecking parameter, k_1	$9.4{\cdot}10^{8}$–$1.5{\cdot}10^{9}$ [m^{-1}]	Fitted
Thermal stress, $\hat{\tau}$	115 [MPa]	Fitted

compared to the total measured value. Other parameters are fitted to correctly reproduce the true stress–strain curves (σ - ϵ) shown in Fig. 9. The simulations of uniaxial tension were performed in the standalone mode described in Section 2.2.2, so no geometrical parameters were given to the model. Deformation time was chosen to replicate the experimental strain rate of $2.78 \cdot 10^{-4}$ s^{-1} (10% of total deformation in 360 s). The virtual polycrystal consisted of 50 randomly oriented grains. This amount was confirmed to provide a comparable output to the case of 1000 randomly oriented grains (maximum difference is less than 2%). A summary of the described parameters is provided in Table 5. The resulting material laws compared to the experimental curves are shown in Fig. 10.

3.1.1. Radiation-affected material laws

To establish the material laws of the radiation-affected subsurface and simulate irradiation hardening, the dpa dose distribution along the irradiated area of the NI specimen must be divided into distinct layers and analyzed, see Fig. 1. The constitutive parameter S_{irr} from Eq. (2) is parameterized to associate yield stress and indentation hardness with a certain level of the damage dose. To this end, the S_{irr} values are fitted to the yield stresses from the real tensile tests of neutron-irradiated Eurofer97 as taken from [57]. Then, the established constitutive laws are transferred to the subsurface layers of the specimen box to simulate the ion-irradiated material. In replication of the experimental NI data, the interconnection between irradiation hardening levels caused by ions and neutrons is established through the modified material laws.

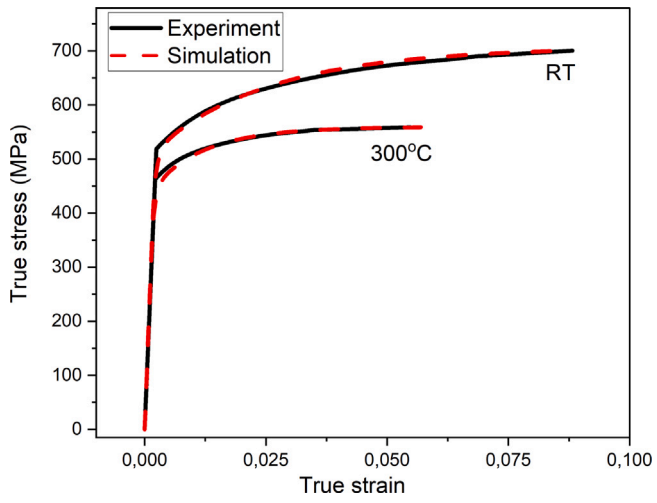

Fig. 10. Simulated and experimental true stress–strain curves of Eurofer97 in comparison.

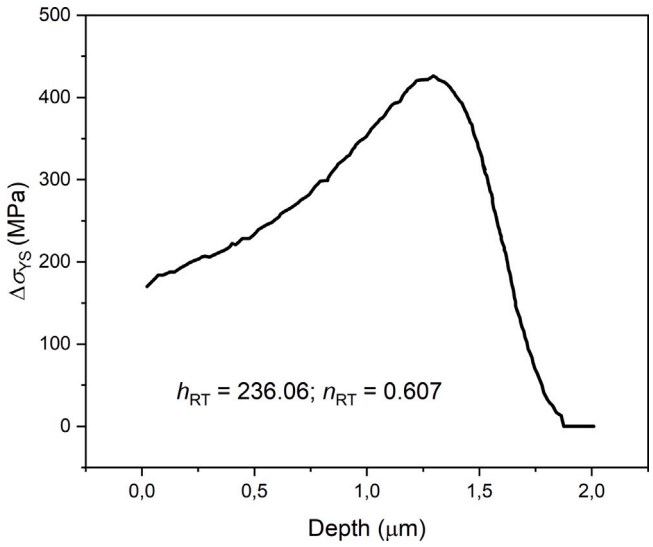

Fig. 11. The magnitude of irradiation hardening in ion-irradiated Eurofer97 with respect to depth.

To associate radiation-induced hardening (in terms of yield stresses) with the damage dose, the following formula has been used:

$$\Delta\sigma_{YS} = hd^n \tag{7}$$

where $\Delta\sigma_{YS}$ is the magnitude of irradiation hardening (the difference between yield stresses of the reference and irradiated materials) in MPa, d is the displacement damage dose in dpa, h and n are the fit parameters. This power-law expression is one of the simplest models for the irradiation hardening [83]. To find the $\Delta\sigma_{YS}$ values to be applied in the simulations of the NI process, the data from the tensile tests performed on the neutron-irradiated Eurofer97 from [57] were used.

Now, the power law regression method can be used to deduce the h and n parameters to establish the power law relationship and apply it to the ion irradiation damage-depth profile presented in Fig. 4. This provides the distribution of the irradiation hardening along the subsurface of the ion-irradiated NI specimen through the correlation between the yield stress increases and the damage doses. Fig. 11 shows the distribution of irradiation hardening due to the variable damage dose introduced by the ion irradiation. Since only four layers were chosen to mimic hardening (Fig. 1), the displacement damage is differentiated and averaged by layers of 0.5 μm depth, as presented in Fig. 12. Then the S_{irr} parameter is parameterized by performing simulations of the uniaxial tension in the stand-alone mode. This allows obtaining yield stresses at these averaged dose levels, in accordance with the experimental data from [57]. It can be seen that the peak dose of 2.3 dpa in the Layer 3 in Fig. 12 is higher than the available data provided in [57]. Therefore, the corresponding yield stress is extrapolated according to the power law applied to establish the hardening-depth profile (Fig. 11). Once experimentally validated, this may indicate the predictive capability of the method. It should be mentioned that irradiation hardening is known to saturate at higher damage doses [84]. Hence, if higher damage doses are used in this method, more advanced models of irradiation hardening accounting for saturation can be used instead of Eq. (7), see for example [83].

Fig. 13 complies the true stress–strain curves simulated using the stand-alone mode according to the experimental data from [57]. It is important to understand that irradiation damage causes not only irradiation hardening, but also a reduction of uniform and total elongation [85,86], so the constitutive laws presented in Fig. 13 are not completely representative of the plastic deformation mode. This work, however, focuses on the application of NI as the primary experimental technique capable of measuring hardness, which is closely related to the yield stress. There is no simple way to estimate the plastic behavior using self-similar NI with the Berkovich indenter.

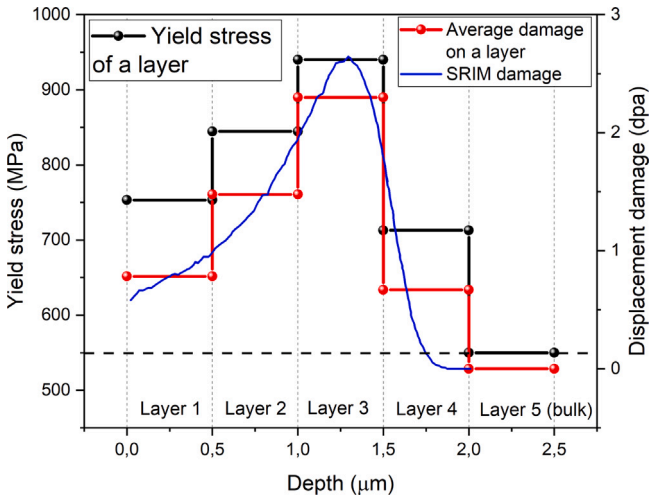

Fig. 12. The damage-depth profile from SRIM (blue) (Fig. 4), averaged damage dose in dpa at each layer (red), and the corresponding yield stress (black). The horizontal dashed line stands for yield stress at 0 dpa. (For interpretation of the references to colour in this figure legend, the reader is referred to the web version of this article.)

The obtained S_{irr} values are given in Fig. 14 and Table 6. The trend reflected in Fig. 14 is correct, as the CRSS depends on the density of irradiation-induced defects, which increases with increasing damage dose.

3.2. Nanoindentation simulations

3.2.1. FEM setup

To simulate the NI process in ion-irradiated material, the FEM setup described in Section 2.2 was developed. The dimensions of the specimen box were chosen as 50 × 50 × 15 μm^3. The 2 μm deep subsurface was divided into four layers (see Fig. 16), which represents the volume affected by ions. Each layer of 0.5 μm and is assigned with a different material law. The established FEM model is shown in Fig. 15. A mesh was generated with refinement in the deforming area achieved using two spherical mesh fields of different radii (see Fig. 16). The first sphere has a radius of 1.3 μm and a characteristic element length of

Table 6
Yield stresses and the corresponding S_{irr} values with respect to the damage dose and a layer.

Layer	Volumetric averaged damage dose, [dpa]	Yield stress, [MPa]	S_{irr}, [MPa]
1 (surface)	0.785	753	90
2	1.5	845	150
3	2.3	940	250
4	0.67	713	70
5 (bulk)	0	550	0

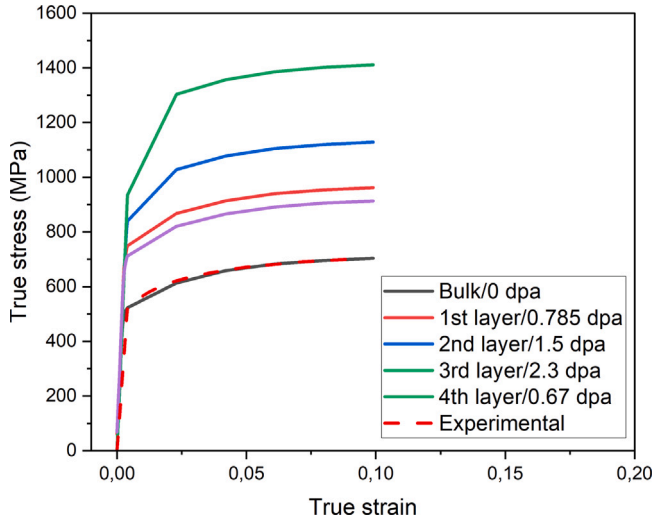

Fig. 13. True stress–strain curves obtained from uniaxial tension simulations in the stand-alone mode. The S_{irr} parameter is being fit until the yield stress at a certain dose is reproduced.
Source: The yield stress values are taken from Ref. [57].

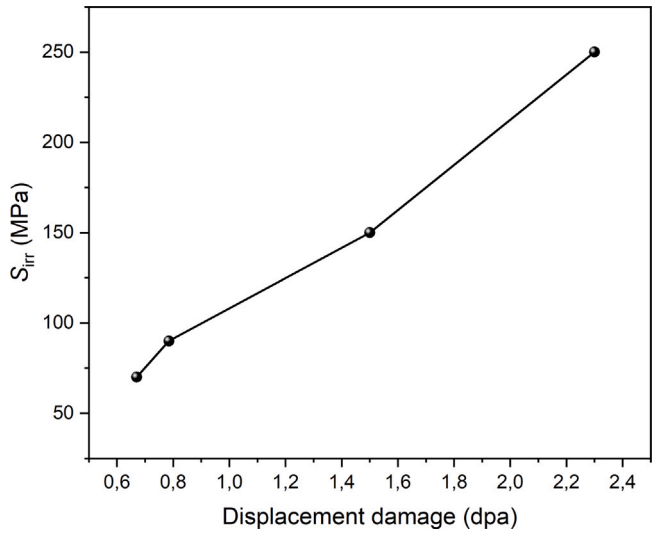

Fig. 14. Stress contribution from the irradiation hardening to the CRSS in a slip system α.

0.125 μm (to improve accuracy at shallow depths), while the second sphere has a radius of 6 μm and a characteristic element length of 0.25 μm (to balance between accuracy and CPU resources). The volume of the specimen box where no deformation is expected seamlessly transitions to the elements with a characteristic element length of 5 μm at maximum. Eventually, the applied mesh consists of 221 273 1st-order tetrahedral elements, where locking is avoided by averaging the volumetric deformation. The simulation was carried out along the surface orientations [100], [101], and [111], and the responses were averaged. This method allows analyzing the deformation process with respect to the principal crystal orientations, while the averaged force–displacement curve is more statistically accurate, than a single one. This approach can be commonly found in the literature [29,32,87].

3.2.2. Simulations results

By applying the FEM setup presented in Section 3.2.1, the NI tests were simulated. For the reference material, each layer was assigned with the same material law derived from the tensile tests performed on non-irradiated material presented in Sections 3.1.1 and 2.3.3. To simulate the ion-irradiated material, the layers were assigned with the corresponding combination of damage dose and constitutive law, as previously described in Section 2.1. The resulting force–displacement curves were obtained with respect to the three principal crystal orientations and then their averaged response was compared with the experimental data, as presented in Fig. 17. The x error bar indicates the scatter between individual NI cycles.

In [62], where the same computational framework was applied to simulate the NI process in pure iron, the similarity between simulation vs. experimental couples of force–displacement curves was discussed. It was pointed out that these couples have different intermediate curvatures (between 0 and h_{max}) of the curves due to the indentation size effect (ISE) coming from the coarse microstructure. In this way, the material response at shallow depths was noticeably different between the experiment and the simulation, which consequently affected the entire force evolution. In the present work this conclusion is confirmed: in Fig. 17(a) one can see a similar phenomenon, however significantly weaker (i.e., higher similarity). This is meaningful, since Eurofer97 has a fine nanostructure [88–90] compared to the pure iron product from [62], thus the ISE has less of an impact. In [91] a nanoindentation hardness-depth profile for non-irradiated Eurofer97 is obtained with many data points, where the ISE influence is already weak after approximately 200 nm of contact depth. As the impact of the ISE decreases even more after irradiation [92,93] (due to the presence of additional defects, i.e., reduction of the strain gradient length scale), the curvature of the experimental force–displacement curve closely approaches that of simulations, where the ISE is absent at all. This assumption is verified in Fig. 17(b).

To calculate the hardness–depth profiles obtained by FEM, the simplified hardness formula was used in [62]:

$$H = \frac{F}{24.56h^2} \tag{8}$$

In this equation, the total depth h is used instead of the contact depth h_c to calculate the indent projection area. This substitution is justified by two facts: first, the simulations were performed using an ideal perfectly sharp Berkovich indenter; second, the contact depth and total depth values calculated experimentally were found to differ only by ~6% in the case of steels, which is small enough for avoiding extra complexity in the hardness equation. When the hardness profiles are compared to the experimental single cycle indentations at two different depths and, as shown in Fig. 18, one notes a good match between the simulated curves and the experimentally obtained values. The difference does not exceed 9%. It may be noted that if the contact depth was used instead of the maximum depth ($h_c < h_{max}$) in the hardness calculations (Eq. (8)), this would give a shift-up of the simulated hardness–depth curves along the y axis, making them match more the 100 mN results, but being higher than the 20 mN results. To minimize these incompatibilities, it

Table 7
The plastic zone radius to indentation depth ratios r_z/h for both states of the material at h = 150 nm. Plastically deformated regions are determined through the accumulated slip $\dot{\Gamma}$ and 0.2% of equivalent strain ϵ_{eq}.

Surface orientation	$r_z/h(\dot{\Gamma})$, reference	$r_z/h(\dot{\Gamma})$, irradiated	$r_z/h(\epsilon_{eq})$, reference	$r_z/h(\epsilon_{eq})$, irradiated
[100]	8.31	6.63	6.89	6.07
[101]	12.06	9.06	10.0	8.3
[111]	11.3	8.73	9.73	7.86
Averaged	10.56 ± 1.95	8.14 ± 1.01	8.87 ± 1.38	7.41 ± 1.15

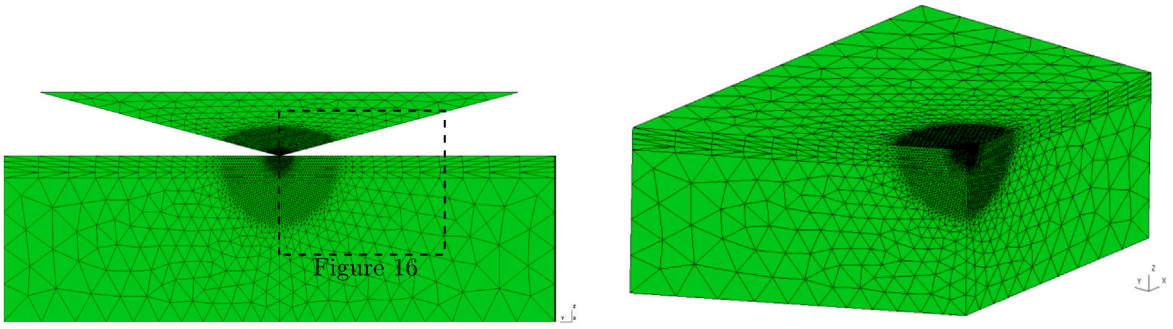

(a) Half-cut side view. (b) Inside view (the indenter is removed).

Fig. 15. Geometry and meshing of the FEM setup of the ion-irradiated specimen shown from different views.

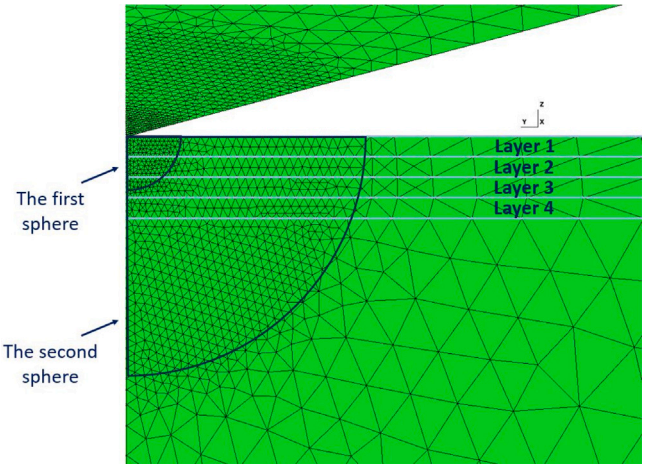

Fig. 16. Geometry and meshing of the layered FEM setup.

is recommended to use the difference between the irradiated and reference curves for comparison, as demonstrated in Fig. 19. Apparently, analyzing radiation-induced hardening as the difference in hardness in the irradiated and reference states seems to be the most meaningful way to use this approach. So that:

$$H_{irr} - H_{ref} = H_{dpa} \tag{9}$$

where H_{dpa} is the radiation-induced hardening, and H_{irr} and H_{ref} are the absolute hardness values for both states of the material.

One may also note in Fig. 18 a slight increase of hardness at lower depths for the reference curve. This effect may be mistakenly considered as the indentation size effect; however, it is an effect of elasticity contributing to the calculated hardness. At the initial stages of indentation, the number of plastically deformed elements is relatively low, so the deformation is primarily accumulated elastically. The material elastic stiffness is significantly higher than plastic, so the overall system response appears stiffer, and the calculated hardness is higher. A mesh convergence study was performed to minimize the elastic contribution, while keeping a reasonable calculation time. This way the mesh described in Section 3.2.1 was established. Eventually, this effect of elasticity is not a major issue, as by affecting both irradiated and references curves it is being neglected when H_{dpa} is used.

3.2.3. Analysis of FEM maps

FEM maps with distributions and magnitudes of important quantities associated with mechanical deformation are analyzed. In Fig. 20 distributions of accumulated slip are given for the case of [110] surface orientation. These maps are used to visualize the extend of the plastic zone beneath the indenter. Elements that have undergone at least 0.001 deformation as accumulated slip are shown. This threshold was chosen to identify regions where plastic deformation has occurred, and lower values did not significantly extend the plastic zone further. The indentation depth equals to 150 nm for both cases.

The extensions of the plastic zones are measured directly from the FEM maps along the z-direction (beneath the indenter), yielding 1809 nm for the reference case and 1359 nm for the irradiated case. This corresponds to plastic zone radius-to-indentation depth ratios r_z/h of 12.06 and 9.06, respectively, at h = 150 nm indentation depth. The values are slightly higher than the commonly accepted range of 5–10 for metals [94,95]. However, this factor is typically estimated using Hertzian contact theory and Von Mises criterion, with the engineering approximation of plasticity defined as 0.2% of equivalent strain. In the presented work, the plasticity is determined as the occurrence of accumulated slip, i.e., the regions where the conditions for plastic slip has been satisfied. This determination is arguably more precise than the 0.2% threshold, allowing to allocate plastic deformation beyond this boundary, resulting in a larger plastic zone.

The reported accumulated slip values can be approximately converted to a quantity analogous to the equivalent strain using the formula that relates strain with slip through the Taylor factor [96]:

$$\dot{M}\epsilon_{eq} = \dot{\Gamma} \tag{10}$$

Here the averaged Taylor factor value of 3 is used for simplicity. However, this factor actually varies with crystal orientation and activated slip systems, what should be noted if more precise recalculation is required. The obtained r_z/h values are listed in Table 7.

A reduction in the plastic zone with irradiation is clearly observed. This behavior is expected, as the irradiation-hardened substrate impedes dislocation movement, thus reducing the material's ability to plastically deform. Moreover, the averaged $r_z/h(\epsilon_{eq})$ for the reference material is in a good agreement with the value reported in [91], where

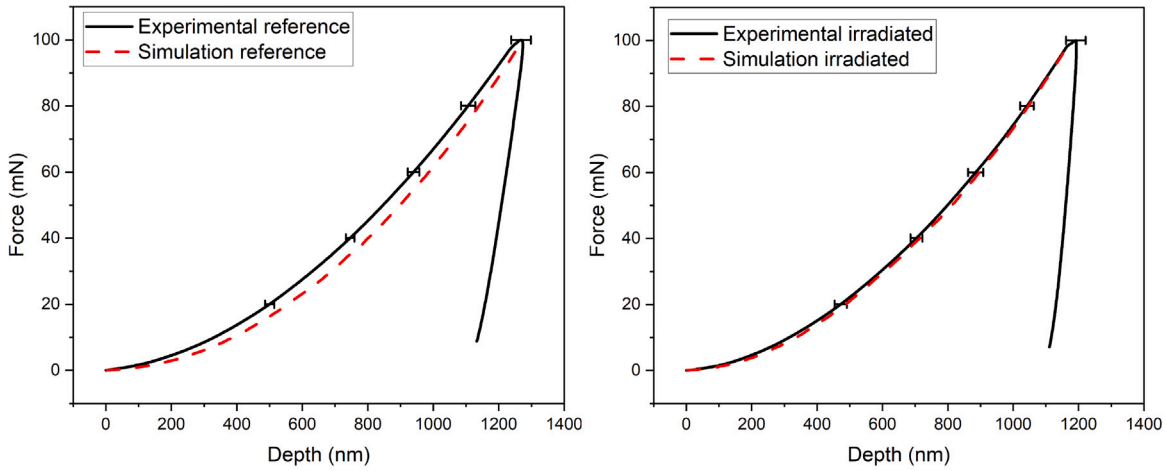

(a) Reference. (b) Irradiated.

Fig. 17. Force–displacement curves for the reference and ion-irradiated Eurofer97 from FEM and experiments.

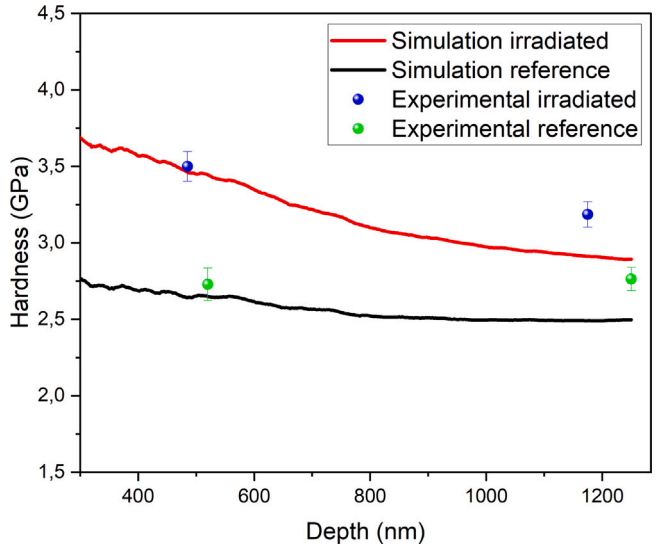

Fig. 18. Hardness–depth profiles from the simulations compared to the experimental single cycle measurements.

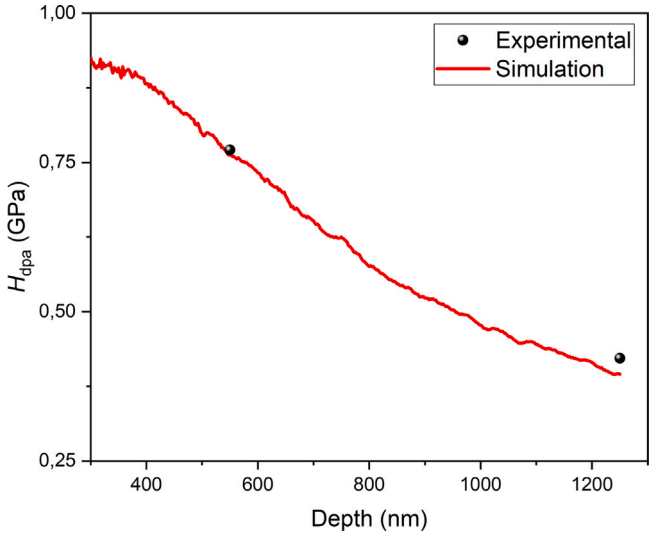

Fig. 19. Difference between hardness of the reference and the irradiated material (radiation-induced hardening).

the plastic zone radius-to-indentation depth ratio for Eurofer97 was obtained analytically by fitting experimental data to a model.

The plastic zone remains constrained until approximately $h = 250$ nm. Beyond this indentation depth, critical stresses reach the non-irradiated bulk, which begins to deform rapidly, causing r_z/h values in the irradiated material to match or even exceed those of the reference case. However, the plastic zone of the ion-irradiated material remains constrained on the xy-plane on the hardened substrate. Fig. 21 presents the accumulated slip maps at $h = 1250$ nm. Although r_z becomes larger in the irradiated material, it is still possible to estimate the plastic zone size by measuring r_y instead. As the deformed zone is not symmetrical, r_y is measured in both directions and then averaged. For the [111] surface orientation the average r_y is 12 000 nm in the reference case and 10 950 nm in the irradiated case, corresponding to r_y/h values of 9.6 and 8.76, respectively (or 8.04 and 7.4 when expressed in terms of ϵ_{eq}).

Although this ratio may vary depending on the layer selected for measurement (due to different degrees of hardening) the main conclusion remains: the irradiated substrate effectively constrains plastic zone expansion, and the resulting r/h values are consistent with those reported in the literature.

The distributions of the dislocation densities at $h = 1250$ nm are given in Fig. 22, where the scale bars for the heights of the specimen and the irradiated subsurface can be seen in Figs. 22(a) and 22(b), 22(d), 22(f), respectively. The first thing observed is that the evolution of the dislocation density is suppressed in the area where the irradiation hardening is present. This shrinks the dislocation forest, making its distribution more concentrated around the indenter tip (indicated by the red arrows in Figs. 22(b), 22(d), 22(f)). Further observation is that the dislocation density evolution propagates deeper into the specimen, once it passes through the hardened subsurface. The parallel red lines between each pair of pictures show that the magnitudes of deformation in the reference material develop less deep than those in the irradiated one. It seems that the dislocations accumulate in the irradiated zone until the stress required to pass it is reached. Then, its evolution concentrates in the less hardened zone (bulk), whereas in the case of the reference material, it can propagate along the surface, reducing its own ability to propagate into bulk. These observations are similar to the behavior of accumulated slip.

The introduction of ion-induced defects activates two competing mechanisms in the dislocation dynamics: (1) defects act as additional obstacles impeding dislocation motion; and (2) they may also serve as

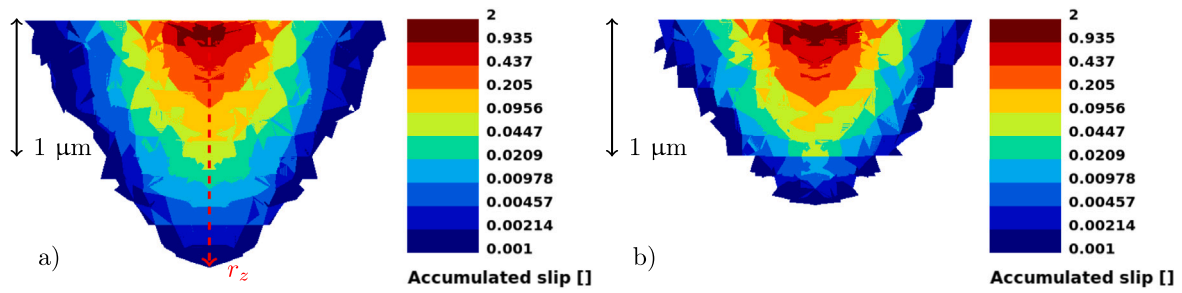

Fig. 20. Distributions of accumulated slip (log scale) at $h = 150$ nm for [110] surface orientation from FEA: (a) reference; (b) ion-irradiated.

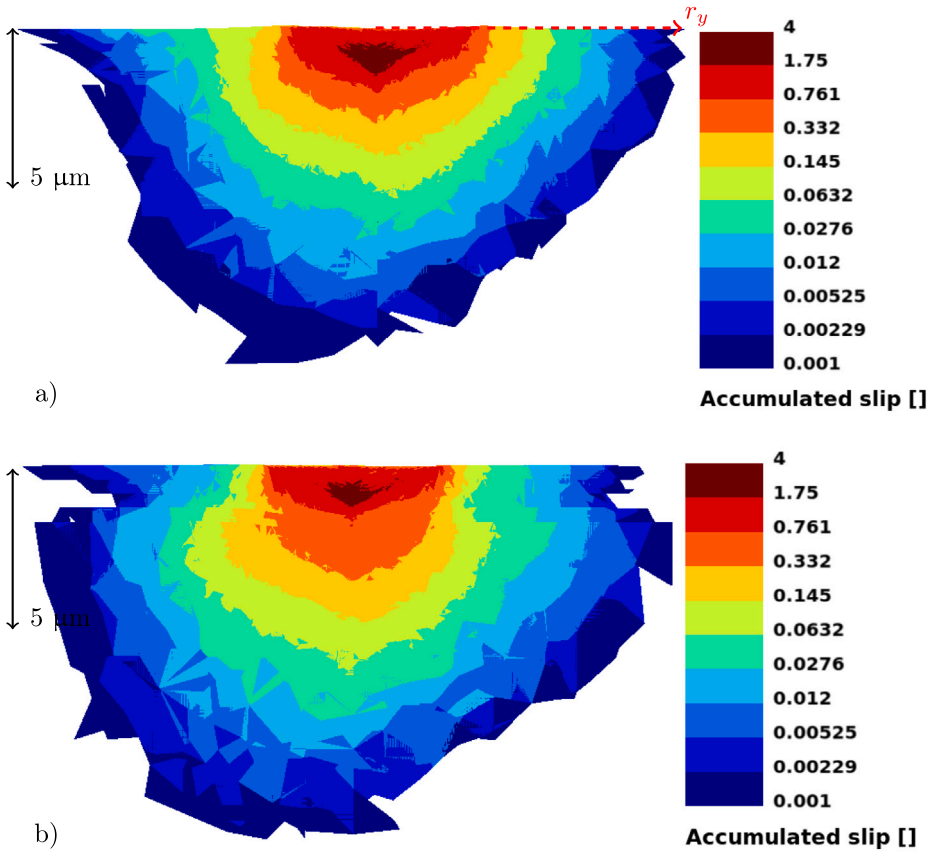

Fig. 21. Distributions of accumulated slip (log scale) at $h = 1250$ nm for [111] surface orientation from FEA: (a) reference; (b) ion-irradiated. (For interpretation of the references to colour in this figure legend, the reader is referred to the web version of this article.)

additional Frank-Read sources, enhancing the ability of the dislocation network to evolve. TEM analysis of the indented regions is required to evaluate the prevailing process for the given irradiation and testing conditions, which is planned as future work. Such analysis will help to evaluate the predictive capability of the approach. Depending on the results, the model may require further improvements in the representation of the irradiated zone. This can be achieved either by adjusting additional constitutive parameters responsible for dislocation dynamics (e.g., k_1, k_2, α) within the irradiated layers, or by explicitly implementing a law that accounts for dislocation-defect interactions.

In Fig. 23 the maximum shear stress profiles are provided for $h = 1250$ nm. The maximum shear stress is calculated as the half-difference between the maximum and minimum principal stresses σ_1 and σ_3 obtained from the Cauchy stress tensor $\boldsymbol{\sigma}$:

$$\tau_{\max} = \frac{1}{2}(\sigma_1 - \sigma_3) \tag{11}$$

As expected, the highest stress concentrations are found in the hardened layers. The magnitudes reach approximately 600 MPa in bulk stress, and at least 1200 MPa on the irradiated subsurface, so it more than doubles for these irradiation conditions. Favorable directions for stress propagation are aligned with slip systems.

4. Discussion

The present approach is semi-empirical. While based on an analytical formulation for the dislocation dynamics, no equations were introduced for the behavior of irradiation defects, their densities, or types. Therefore, the S_{irr} parameter is used to reproduce the magnitude of irradiation hardening only empirically. Indeed, an introduction of such equations could increase the accuracy of the results, and make the description of different hardening phenomena more fundamental and distinguishable; however, working in the way presented significantly reduces the complexity of this predictive technique. It also allows to avoid complex investigations of the irradiated microstructure, reducing the entry threshold of the method application. Under the conditions

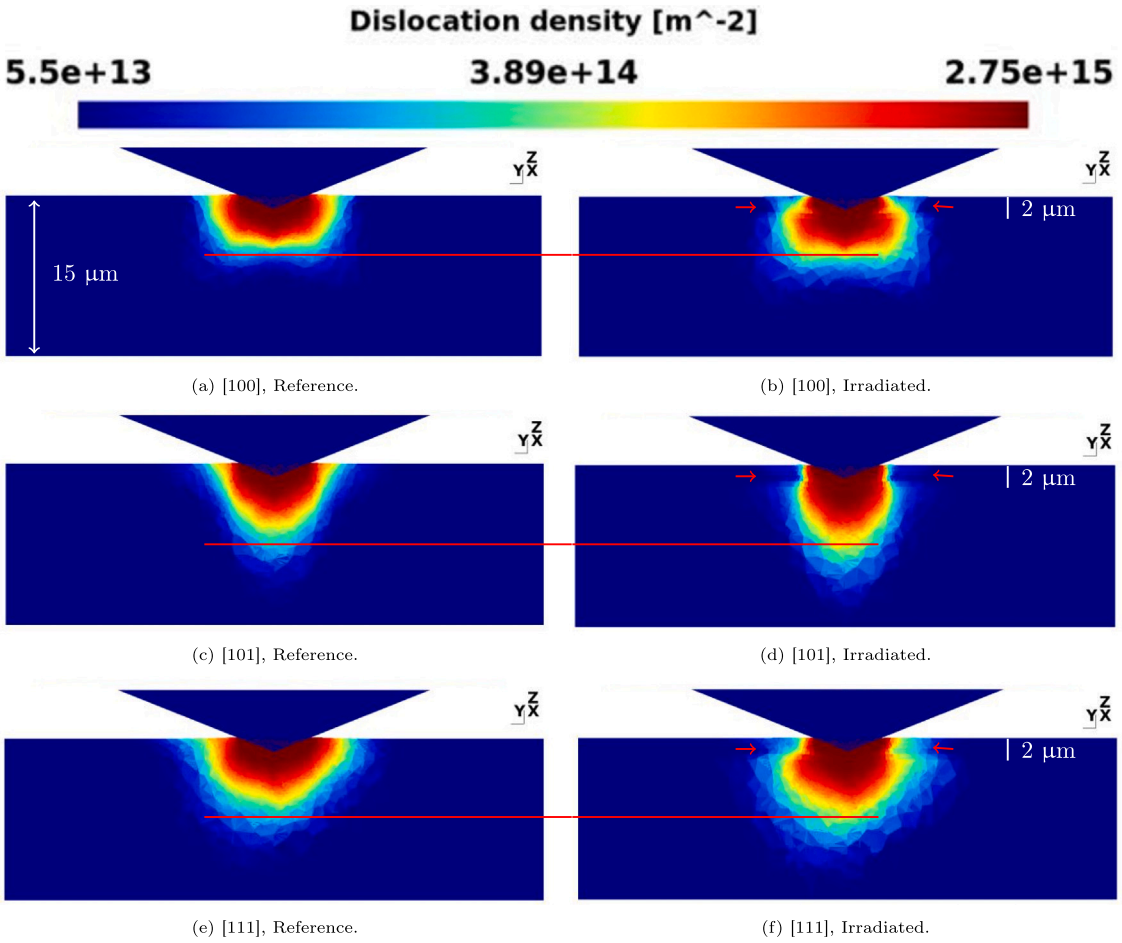

(a) [100], Reference. (b) [100], Irradiated.

(c) [101], Reference. (d) [101], Irradiated.

(e) [111], Reference. (f) [111], Irradiated.

Fig. 22. Dislocation density distributions (log scale) at h_{max} for different surface orientations from FEA. (For interpretation of the references to colour in this figure legend, the reader is referred to the web version of this article.)

presented, the predictive capability of the method appears to be sufficient enough to rely only on the empirical response. Nevertheless, the accuracy of the model can be further assessed by performing TEM of irradiated and deformed samples, comparing the microscopy results with the computational output. This may confirm the necessity to implement additional models describing dislocation-defect interactions to more precisely capture the processes occurring in the irradiated layers. The TEM analysis is included in the scope of the future work. Besides, the predictive capability of the method is likely expected to vary with the material type. Therefore, its applicability should be investigated for other nuclear materials, which is planned for further work. An ideal candidate for this would be tungsten, a fusion-related structural material that has been extensively studied after ion and neutron irradiation and frequently modeled using CPFEM approaches, including a framework similar to the one employed in this study [97].

At the same time, the computational framework lacks an implementation of additional models capable of simulations of the indentation size effects. The magnitude of irradiation hardening can be estimated incorrectly at shallow depths, and in materials where the ISE is high. Therefore, the presented CPFEM framework could benefit from additional control on the physical phenomena affecting the NI process. Specifically, a strain gradient plasticity model could not only account for the ISE, but also allow the polycrystalline microstructure to be correctly simulated, noting that the Hall-Petch effect may be attributed to strain gradient effects at the grain interfaces. Taking into account the scales of grain boundary strengthening in materials with fine microstructure and the scales of the indentation size effect in materials with coarse microstructure, as well as the impact of both phenomena on the NI process, the implementation of a strain gradient plasticity model is considered priority for a further development of the present method.

When NI analysis of ion-irradiated materials is discussed, the real interest and ultimate goal is to use it to predict the effect of neutron damage. The present research establishes the reversed procedure: when knowledge of the impact of neutron damage allows the performance of an ion-irradiated material to be reproduced. This allows validating the approach, but, on the other hand, it cannot be applied practically. A direct method is crucial to make this approach useful in real applications. To demonstrate the direct method, manual fitting can be used. The S_{irr} parameter at each layer is manually fitted to obtain a good reproduction of the experimental NI hardness–depth functions (Fig. 24(a)), and then used to simulate the uniaxial tensile tests to mimic the neutron-irradiated material. Fig. 24(b) shows yield stresses obtained experimentally on the neutron-irradiated material compared to yield stresses from the present approach as applied to the ion-irradiated material. The predictive capability is summarized in Table 8, where relative errors (RE) are calculated with respect to the total yield stress values (full) and to the magnitudes of irradiation hardening only (i.e., the non-irradiated yield stress value is subtracted) (increase).

Several conclusions can be drawn regarding the demonstrated predictability. Firstly, manual fitting of four closely related parameters (hardness of each layer) is not an efficient procedure. The accuracy provided in Table 8 and in Fig. 24 can be improved by implementing a computational algorithm, which will combine several aspects, such as: fitting of the material laws, transferring them into CPFEM simulations, performing these simulations, and simultaneously analyzing the output

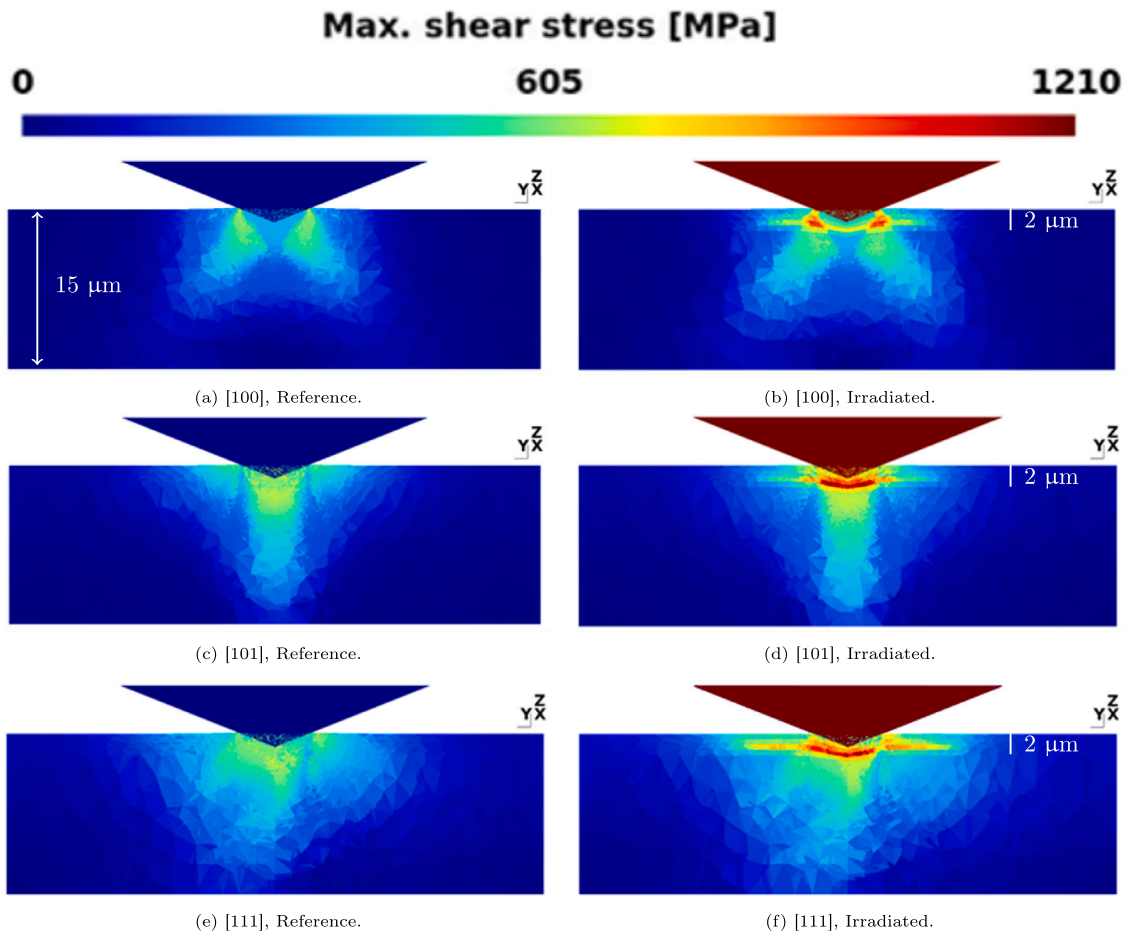

(a) [100], Reference. (b) [100], Irradiated.

(c) [101], Reference. (d) [101], Irradiated.

(e) [111], Reference. (f) [111], Irradiated.

Fig. 23. Maximum shear stress distributions at $h = 1250$ nm for different surface orientations from FEA.

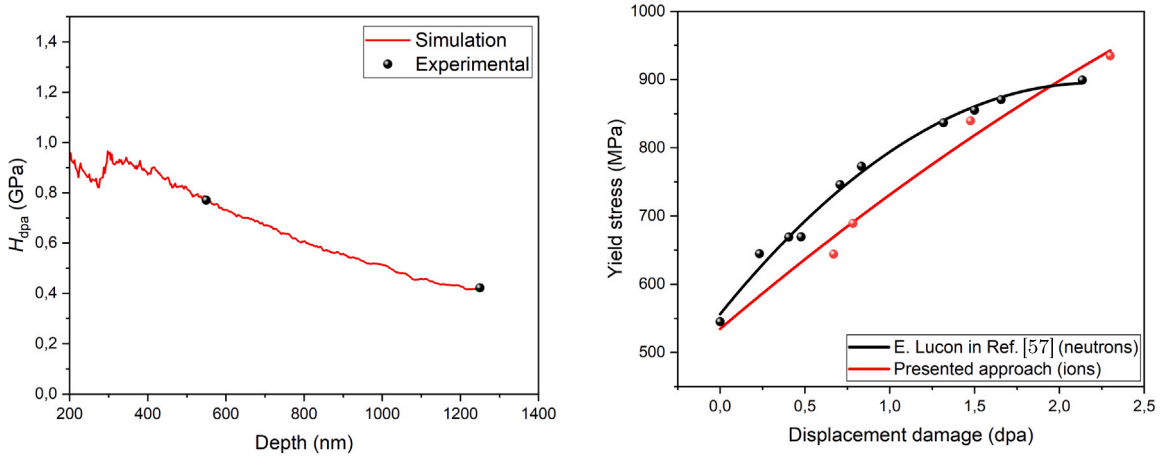

(a) (b)

Fig. 24. (a) Hardness–depth functions obtained experimentally and by manual fitting of S_{irr} in simulations; (b) Experimental yield stresses of neutron-irradiated Eurofer97 in comparison with the presented approach.

Table 8
Predictive capability of the method. S_{irr} is manually fitted to the known distribution of the damage dose from SRIM.

Damage dose, [dpa]	Predicted yield stress, [MPa]	Measured yield stress from [57], [MPa]	Absolute difference, [MPa]	RE (full)	RE (increase)
0.67	645	731	86	11.77%	47.51%
0.785	690	753	63	8.37%	31.03%
1.48	841	860	19	2.21%	6.13%
2.13	920	902	−18	2.0%	5.11%

to be in match with the experimental data; making corrections if the output is outside a certain tolerance, and following the distributions of the damage doses. Such an algorithm can be implemented by using Neural-Network accelerated Bayesian inference of model parameters, where NI hardness–depth curves are used as a surrogate model [98]. Secondly, the observed mismatch, which is especially high for the lower damage doses, can be associated with the differences in the irradiation dose rates: $2.78{\cdot}10^{-5}$ dpa/s for ions versus $1.5{\cdot}10^{-7}$ dpa/s for neutrons. Although the dose rates in this work differ by about 2.3 orders of magnitude (while it can reach even 3–4 orders of magnitude in the literature), such a difference may still lead to a distorted balance in defect formation and precipitation processes. This can be crucial for achieving a representative material state after ion irradiation to neutron irradiation, so lowering ion dose rates or increasing ion irradiation temperature is recommended. Overall, other irradiation parameters, such as damage dose and temperature may also affect the predictability of the method. The former is known to saturate the hardening effect with its increase, which means that the presented method is only working up to a certain dose level, specific for each material. However, it may be still applicable within a certain range of doses even close to the saturation, but where the difference in hardness is still distinguishable. This would require employing a more advanced hardening model instead of Eq. (7), which is already being investigated for ion-irradiated Eurofer97 with 5 dpa in peak damage.

The constitutive material law was established for room temperature and 300 °C; therefore, it can be used to perform the nanoindentation CPFEM simulations at elevated temperatures. However, it requires a more complex high temperature NI experimental campaign, which must also account for the irradiation temperature (300 °C in this case) to avoid annealing of the irradiation damage. Overall, the elevated temperature NI tests are of primary interest in this subject, since these conditions represent the real operational environment of nuclear reactors. Validational experiments for the high temperature NI simulations are considered as a follow-up to the present development.

Eventually, a valuable contribution to the presented work would be a nanoindentation campaign performed on neutron-irradiated Eurofer97. This would allow to introduce an intermediate data set to investigate how CPFEM modeling can connect the same modes of deformation under different irradiation types — or conversely, how nanoindentation and tensile testing correlate after neutron irradiation. However, performing nanoindentation on neutron-irradiated materials is extremely challenging, with only few laboratories worldwide equipped with such a setup.

5. Summary & conclusions

In this work, a semi-empirical approach to interconnect the impact of ion and neutron damage on the mechanical properties of the RAFM steel Eurofer97 was introduced. This interconnection is found through the correlations of yield stress and hardness values, which were reproduced in accordance with the corresponding irradiation damage doses. The computational results obtained were experimentally validated. The effect of the ion irradiation damage is incorporated into the CPFEM model via division of the specimen sub-surface into four layers; each assigned with a modified constitutive law representing irradiation hardening with respect to the average dose on the layer. The modifications were performed in accordance with the experimental data obtained from tensile tests on the neutron-irradiated material. It allowed reproducing the experimental NI hardness–depth relationship with an accuracy of less than 9% as absolute values and approximately 6% as the difference between the irradiated and reference hardness–depth curves (radiation-induced hardening). Several conclusions can be drawn:

- The constitutive parameters were obtained on the basis of the literature and fitting to the tensile tests. The dislocation–dislocation interaction factor and the Kocks–Mecking parameter are the only parameters that change with temperature, and this finding is in accordance with the information available in the literature. The initial dislocation density was reduced (from $1.5 \cdot 10^{14}$ to $5.5 \cdot 10^{13}$ m^{-2}), which can be explained by the fact that only a fraction of the entire dislocation forest represents mobile dislocations.
- According to FEM maps of accumulated slip and dislocation density, the plastic zone created by the indenter tip is constrained due to the irradiation; however, this observation is valid at the indentation depths lower than 250 nm. At greater depths, plastic deformation starts to propagate to the non-irradiated substrate, what enhances the plastic zone evolution into depth. Nevertheless, in the latter case plasticity is still constrained along the surface, where the hardened layers are present. The degrees of the contraction correlate with the ones commonly reported in the literature.
- When analyzing and comparing the hardness obtained both computationally and experimentally, it is more accurate and meaningful to use their differences H_{dpa}, rather than the absolute values. It allows suppressing any experimental and modeling artifacts which are not associated with the effect of irradiation (assuming them to be equally inherent for each irradiated-reference couple of curves). However, the usage of H_{dpa} is justified only in the case when the absolute values are also in an acceptable comparable range.
- The predictive capability of the method must be further investigated, as it is likely dependent on material type and irradiation parameters. Moreover, ion irradiation dose rates are significantly higher that the neutron ones, what may lead to a different nature of damage accumulation. The approach should be applied to other irradiated materials and irradiation parameters, what is partially ongoing as a follow-up to this work.
- Developing a direct algorithm to efficiently fit the irradiation hardening parameter S_{irr} to the complex dpa–hardness–depth profile is necessary to improve the accuracy and eliminate manual fitting.

Declaration of competing interest

The authors declare the following financial interests/personal relationships which may be considered as potential competing interests: Tymofii Khvan reports financial support was provided by National Science Centre Poland. If there are other authors, they declare that they have no known competing financial interests or personal relationships that could have appeared to influence the work reported in this paper.

Acknowledgment

This work has been carried out within the framework of the EUROfusion Consortium, funded by the European Union via the Euratom Research and Training Programme (Grant Agreement No 101052200 — EUROfusion). Views and opinions expressed are however those of the author(s) only and do not necessarily reflect those of the European Union or the European Commission. Neither the European Union nor the European Commission can be held responsible for them.

The experimental data used in this research were collected through access to the Micro-Characterisation Laboratory (MCL) under the framework of Open Access to the Joint Research Centre Physical Research Infrastructures of the European Commission (Project NIFEM, Research Infrastructure Access Agreement N° 2020-1-RD-EMMA-MCL-36044-1).


This research is part of the project No. 2022/47/P/ST5/01169 co-funded by the National Science Centre and the European Union

Framework Programme for Research and Innovation Horizon 2020 under the Marie Skłodowska-Curie grant agreement No. 945339. For the purpose of Open Access, the author has applied a CC-BY public copyright license to any Author Accepted Manuscript (AAM) version arising from this submission. The publication was created within the framework of the project of the Minister of Science and Higher Education "Support for the activities of Centres of Excellence established in Poland under Horizon 2020" under contract no. MEiN/2023/DIR/3795. We also acknowledge support from the European Union Horizon 2020 research and innovation program under grant agreement no. 857470, the European Regional Development Fund via the Foundation for Polish Science International Research Agenda PLUS program grant No. MAB PLUS/2018/8.

Data availability

Data will be made available on request.

References

[1] Garner F, Hamilton M, Panayotou N, Johnson G. The microstructural origins of yield strength changes in aisi 316 during fission or fusion irradiation. J Nucl Mater 1981;104:803–7.
[2] Odette G, Lucas G. Recent progress in understanding reactor pressure vessel steel embrittlement. Radiat Eff Defects Solids 1997;144(1–4):189–231.
[3] Gaganidze E, Aktaa J. Assessment of neutron irradiation effects on RAFM steels. Fusion Eng Des 2013;88(3):118–28.
[4] Slugeň V, Sojak S, Egger W, Krsjak V, Veternikova J, Petriska M. Radiation damage of reactor pressure vessel steels studied by positron annihilation spectroscopy—A review. Met 2020;10.
[5] Wakai E, Takaya S, Matsui Y, Nagae Y, Kato S, Suzudo T, Yamaguchi M, Aoto K, Nogami S, Hasegawa A, Abe H, Sato K, Ishida T, Makimura S, Hurh PG, Ammigan K, Se DJ. Irradiation damages of structural materials under different irradiation environments. J Nucl Mater 2021;543.
[6] Zinkle S, Maziasz P, Stoller R. Dose dependence of the microstructural evolution in neutron-irradiated austenitic stainless steel. J Nucl Mater 1993;206(2–3):266–86.
[7] Hosemann P. Small-scale mechanical testing on nuclear materials: bridging the experimental length-scale gap. Scr Mater 2018;143:161–8.
[8] Zheng P, Chen R, Liu H, Chen J, Zhang Z, Liu X, Shen Y. On the standards and practices for miniaturized tensile test—A review. Fusion Eng Des 2020;161.
[9] Gianola DS, della Ventura NM, Balbus GH, Ziemke P, Echlin MP, Begley MR. Advances and opportunities in high-throughput small-scale mechanical testing. Curr Opin Solid State Mater Sci 2023;27(4):101090.
[10] Zinkle S, Busby J. Structural materials for fission & fusion energy. Mater Today 2009;12.
[11] Ortner S. A review of structural material requirements and choices for nuclear power plant. Front Nucl Eng 2023;2.
[12] Was G. Challenges to the use of ion irradiation for emulating reactor irradiation. J Mater Res 2015;30:1158–82.
[13] Worrall M, Woolstenhulme N, Downey C, Jesse C, Murdock C, Tippet M. Fast neutron irradiation capability in existing thermal test reactors. Ann Nucl Energy 2024;207:110731.
[14] Nordlund K, Sand AE, Granberg F, Zinkle SJ, Stoller R, Averback RS, Suzudo T, Malerba L, Banhart F, Weber WJ, Willaime F, Dudarev S, Simeone D. Primary radiation damage in materials. Review of current understanding and proposed new standard displacement damage model to incorporate in cascade defect production efficiency and mixing effects. Tech. rep., IAEA; 2015, OECD/NEA.
[15] Nordlund K, Zinkle S, Sand A, Granberg F, Averback R, Stoller R, Suzudo T, Malerba L, Banhart F, Weber W, Willaime F, Dudarev S, Simeone D. Primary radiation damage: A review of current understanding and models. J Nucl Mater 2018;512:450–79.
[16] Ullmaier H. Radiation damage in metallic materials. MRS Bull 1997;22:14–21. http://dx.doi.org/10.1557/S088376940003298X.
[17] Robinson M. Basic physics of radiation damage production. J Nucl Mater 1994;216:1–28. http://dx.doi.org/10.1016/0022-3115(94)90003-5.
[18] Spitsyn A, Bobyr N, Kulevoy T, Fedin P, Semennikov A, Stolbunov V. Use of MeV energy ion accelerators to simulate the neutron damage in fusion reactor materials. Fusion Eng Des 2019;146:1313–6. http://dx.doi.org/10.1016/j.fusengdes.2019.02.065.
[19] ASTM International. Standard practice for investigating the effects of neutron radiation damage using charged-particle irradiation. 2023.
[20] Brinkman J. On the nature of radiation damage in metals. J Appl Phys 1954;25:961–70. http://dx.doi.org/10.1063/1.1721810.
[21] Heintze C, Recknagel C, Bergner F, Hernández-Mayoral M, Kolitsch A. Ion-irradiation-induced damage of steels characterized by means of nanoindentation. Nucl Instrum Methods Phys Res Sect B 2009;267(8–9):1505–8. http://dx.doi.org/10.1016/j.nimb.2009.01.122.
[22] Gilbert M, Dudarev S, Nguyen-Manh D, Zheng S, Packer L, Sublet J-C. Neutron-induced dpa, transmutations, gas production, and helium embrittlement of fusion materials. J Nucl Mater 2013;442(1–3):S755–60. http://dx.doi.org/10.1016/j.jnucmat.2013.03.085.
[23] Hardie CD, Williams CA, Xu S, Roberts SG. Effects of irradiation temperature and dose rate on the mechanical properties of self-ion implanted Fe and Fe–Cr alloys. J Nucl Mater 2013;439(1–3):33–40.
[24] Taller S, Vancoevering G, Wirth B, Was G. Predicting structural materials degradation in advanced nuclear reactors with ion irradiation. Sci Rep 2021;11:2949.
[25] Malerba L, Caturla M, Gaganidze E, Kaden C, Konstantinović M, Olsson P, Robertson C, Rodney D, Ruiz-Moreno A, Serrano M, Aktaa J, Anento N, Austin S, Bakaev A, Balbuena J, Bergner F, Boioli F, Boleininger M, Bonny G, Castin N, Chapman J, Chekhonin P, Clozel M, Devincre B, Dupuy L, Diego G, S.L. D, Fu C-C, Gatti R, Gélébart L, Gómez-Ferrer B, Gonçalves B, Guerrero C, Gueye P, Hähner P, Hannula S, Hayat Q, Hernández-Mayoral M, Jagielski J, Jennett N, Jiménez F, Kapoor G, Kraych A, Khvan T, Kurpaska L, Kuronen A, Kvashin N, Libera O, Ma P-W, Manninen T, Marinica M-C, Merino S, Meslin E, Mompiou F, Mota F, Namburi H, Ortiz C, Pareige C, Prester M, Rajakrishnan R, Sauzay M, Serra A, Simonovski I, Soisson F, Spätig P, Tanguy D, Terentyev D, Trebala M, Trochet M, Ulbricht A, Vallet M, Vogel K, Yalchinkaya T, Zhao J. Multiscale modelling for fusion and fission materials: The M4F project. Nucl Mater Energy 2021;29.
[26] Ziegler J, Ziegler M, Biersack J. SRIM – The stopping and range of ions in matter. Nucl Instrum Methods Phys Res Sect B 2010;268:1818–23.
[27] Cozzarizza D, Corniani E, D'Agata E, Ciolini R, Giusti V. Comparison of Monte Carlo tools for displacement calculations for protons and heavy ions irradiation on iron and EUROFER97. J Eng Mater Technol 2024;146(4). http://dx.doi.org/10.1115/1.4066060.
[28] Lin P, Nie J, Liu M. Study on irradiation effect in stress-strain response with CPFEM during nano-indentation. Nucl Mater Energy 2020;22.
[29] Lin P, Nie J, Liu M. Nanoindentation experiment and crystal plasticity study on the mechanical behavior of Fe-ion-irradiated A508-3 steel. J Nucl Mater 2022;571.
[30] Lin P-d, Nie J-f, Cui W-d, He L, Cui S-g, Xiang L-x, Lu Y-p, Xiao G-y. Experimental and modeling study on irradiation effect of a508-III steel. Int J Mech Sci 2024;277:109371.
[31] Lin P-d, Nie J-f, Cui W-d, He L, Cui S-g, Lu Y-p. Comparative analysis of irradiation-stimulated hardening in the austenite and ferrite phases of F321 stainless steel. Acta Mater 2024;281:120409.
[32] Xiao X, Chen L, Yu L, Duan H. Modelling nano-indentation of ion-irradiated FCC single crystals by strain-gradient crystal plasticity theory. Int J Plast 2019;116:216–31.
[33] Xiao X, Terentyev D, Ruiz A, Zinovev A, Bakaev A, Zhurkin E. High temperature nano-indentation of tungsten: modelling and experimental validation. Mater Sci Eng: A 2019;743:106–13.
[34] Xia L, Mao J, Chen D, Cao Y, Xiao X, Jiang C. Temperature-dependent hardening of zirconium alloys under heavy ion-irradiation: Experimental observation and theoretical analysis. J Nucl Mater 2022;572:153989.
[35] Xia L, Chen Y, Huang J, Wang Y, Wang C, Xue J, Xiao X. Revealing the temperature-dependent hardening mechanisms of non-uniformly distributed defects for ion-irradiated metals: Experiments and modeling. Mater Sci Eng: A 2024;899:146408.
[36] Nie J, Lin P, Liu Y, Zhang H, Wang X. Simulation of the irradiation effect on hardness of Chinese HTGR A508-3 steels with CPFEM. Nucl Eng Technol 2019;51(8):1970–7.
[37] Knapp J, D.M. F, Myers S, Barbour J, Friedmann T. Finite-element modeling of nanoindentation. J Appl Phys 1999;85:1460–74.
[38] Su Y, Zambaldi C, Mercier D, Eisenlohr P, Bieler T, Crimp M. Quantifying deformation processes near grain boundaries in α titanium using nanoindentation and crystal plasticity modeling. Int J Plast 2016;86:170–86.
[39] Song K, Yu H, Karamched P, Mizohata K, Armstrong DEJ, Hofmann F. Deformation behaviour of ion-irradiated FeCr: A nanoindentation study. J Mater Res 2022;37:2045–60. http://dx.doi.org/10.1557/s43578-022-00511-7.
[40] Zhou D, Spätig P, Hayat Q, Song P, Jennett N, Chen J-C, Desgardin P. Study of the irradiation hardening of a Fe9Cr ferritic model alloy by nanoindentations. Nucl Mater Energy 2024;39:101667.
[41] Hosemann P, Vieh C, Greco R, Kabra S, Valdez J, Cappiello M, Maloy S. Nanoindentation on ion irradiated steels. J Nucl Mater 2009;389:239–47.
[42] Veleva L, Hähner P, Dubinko A, Khvan T, Terentyev D, Ruiz-Moreno A. Depth-sensing hardness measurements to probe hardening behaviour and dynamic strain ageing effects of iron during tensile pre-deformation. Nanomater 2021;11.
[43] Ma H, Fan P, Qian Q, Zhang Q, Li K, Zhu S, Yuan D. Nanoindentation test of ion-irradiated materials: Issues, modeling and challenges. Mater 2024;17(13):3286.

[44] Gaganidze E, Gillemot F, Szenthe I, Gorley M, Rieth M, Diegele E. Development of EUROFER97 database and material property handbook. Fusion Eng Des 2018;135:9–14.
[45] Stornelli G, Di Schino A, Montanari R, Sgambetterra M, Testani C, Varone A. Ultra-fine grained EUROFER97 steel for nuclear fusion applications. J Mater Res Technol 2024;33:5075–87.
[46] Giancarli L, Abdou M, Campbell D, Chuyanov V, Ahn M, Enoeda M, Pan C, Poitevin Y, Kumar ER, Ricapito I, Strebkov Y, Suzuki S, Wong P, Zmitko M. Overview of the ITER TBM program. Fusion Eng Des 2012;87(5–6):395–402.
[47] Federici G, Boccaccini L, Cismondi F, Gasparotto M, Poitevin Y, Ricapito I. An overview of the EU breeding blanket design strategy as an integral part of the DEMO design effort. Fusion Eng Des 2019;141:30–42.
[48] You J, Visca E, Bachmann C, Barrett T, Crescenzi F, Fursdon M, Greuner H, Guilhem D, Languille P, Li M, McIntosh S, Müller A, Reiser J, Richou M, Rieth M. European DEMO divertor target: Operational requirements and material-design interface. Nucl Mater Energy 2016;9:171–6.
[49] Terentyev D, Puype A, Kachko O, Renterghem WV, Henry J. Development of RAFM steel for nuclear applications with reduced manganese, silicon and carbon content. Nucl Mater Energy 2021;29.
[50] Kachko O, Puype A, Terentyev D, Bonny G, Renterghem WV, Petrov R. Development of RAFM steels for high temperature applications guided by thermodynamic modelling. Nucl Mater Energy 2022;32.
[51] Kachko O, Puype A, Terentyev D, Duerrschnabel M, Klimenkov M, Petrov R. TEM investigation of reduced activation ferritic/martensitic alloys developed by thermodynamic modeling. J Nucl Mater 2023;582:154480.
[52] Tan L, Snead L, Katoh Y. Development of new generation reduced activation ferritic-martensitic steels for advanced fusion reactors. J Nucl Mater 2019;478:42–9.
[53] Ge S, Niu B, Wang Z, Wang Q, Pan Q, Liu C, Dong C, Liaw PK. Developing novel high-Si 12% Cr reduced-activation ferritic/martensitic cladding alloys via the cluster-formula approach and calphad method. Mater Des 2025;251:113722.
[54] Tabor D. The hardness of metals. Oxford University Press; 1951.
[55] Atkins A, Tabor D. Plastic indentation in metals with cones. J Mech Phys Solids 1965;13(3):149–64.
[56] Leitner A, Maier-Kiener V, Kiener D. Essential refinements of spherical nanoindentation protocols for the reliable determination of mechanical flow curves. Mater Des 2018;146:69–80.
[57] Lucon E, Chaouadi R, Decreton M. Mechanical properties of the European reference RAFM steel (EUROFER97) before and after irradiation at 300°C. J Nucl Mater 2004;329–333:1078–82.
[58] Geuzaine C, Remacle J. Gmsh: A 3-D finite element mesh generator with built-in pre- and post-processing facilities. Internat J Numer Methods Engrg 2009;79:1309–31.
[59] Noels L. Computational & multiscale mechanics of materials. Aerospace and Mechanical Engineering Department at the University of Liège, [Online]. Available: http://www.ltas-cm3.ulg.ac.be.
[60] Lemoine G, Delannay L, Idrissi H, Colla M, Pardoen T. Dislocation and back stress dominated viscoplasticity in freestanding sub-micron Pd films. Acta Mater 2016;111:10–21.
[61] Lin F, Marteleur M, Jacques P, Delannay L. Transmission of 332<113>twins across grain boundaries in a metastable β-titanium alloy. Int J Plast 2018;105:195–210.
[62] Khvan T, Noels L, Terentyev D, Dencker F, Stauffer D, Hangen U, Renterghem WV, Chang C, Zinovev A. High temperature nanoindentation of iron: Experimental and computational study. J Nucl Mater 2022;567.
[63] Kocks U, Argon A, Ashby M. Thermodynamics and kinetics of slip. Pergamon Press; 1975.
[64] Frost H, Ashby M. Deformation-mechanism maps: The plasticity and creep of metals and ceramics. Pergamon Press; 1982.
[65] Amodeo J, Dancette S, Delannay L. Atomistically-informed crystal plasticity in MgO polycrystals under pressure. Int J Plast 2016;82:177–91.
[66] Ono K. Temperature dependence of dispersed barrier hardening. J Appl Phys 1968;39:1803–6.
[67] Hall E. The deformation and ageing of mild steel: III discussion of results. Proc Phys Soc B 1951;64.
[68] Terentyev D, Xiao X, Dubinko A, Bakaeva A, Duan H. Dislocation-mediated strain hardening in tungsten: thermo-mechanical plasticity theory and experimental validation. J Mech Phys Solids 2015;85:1–15.
[69] Mecking H, Kocks U. Kinetics of flow and strain-hardening. Acta Metall 1981;29:1865–75.
[70] Kocks U. Realistic constitutive relations for metal plasticity. Mater Sci Eng: A 2001;317:181–7.
[71] Taylor G. Plastic strain in metals. J Inst Met 1938;62:307–24.
[72] Rieth M, Schirra M, Falkenstein A, Graf P, Heger S, Kempe H, Lindau R, Zimmermann H. EUROFER 97. Tensile, charpy, creep and structural tests. Technical report FZKA-6911, Forschungszentrum Karlsruhe; 2003.
[73] Stoller R, Toloczko M, Was G, Certain A, Dwaraknath S, Garner F. On the use of SRIM for computing radiation damage exposure. Nucl Instrum Methods Phys Res Sect B: Beam Interact Mater Atoms 2013;310:75–80.
[74] Jenet A, Acosta B, Boboridis K, Colineau E, Colpo P, Fontana C, Heyse J, Hult M, Peroni M, Malkow T, Nilsson K-F, Oberstedt S, Pfrang A, Schillebeeckx P, Tsionis G, Tuček K, Perez-Medina M, Molina F, Taucer F. Open access to JRC research infrastructures: The first five years. Publications Office of the European Union; 2024, http://dx.doi.org/10.2760/69299.
[75] Oliver WC, Pharr GM. An improved technique for determining hardness and elastic modulus using load and displacement sensing indentation experiments. J Mater Res 1992;7:1564–83.
[76] Ruiz-Moreno A, Hähner P, Kurpaska L, Jagielski J, Spätig P, Trebala M, Hannula S-P, Merino S, de Diego G, Namburi H, Libera O, Terentyev D, Khvan T, Heintze C, Jennett N. Round robin into best practices for the determination of indentation size effects. Nanomater 2020;10(1):130.
[77] ASTM International. Standard test methods for tension testing of metallic materials. 2022.
[78] Adams J, Agosta D, Leisure R. Elastic constants of monocrystal iron from 3 to 500K. J Appl Phys 2006;100:113530.
[79] Davey WP. Precision measurements of the lattice constants of twelve common metals. Phys Rev 1925;25:753–61.
[80] Okazaki K. Solid-solution hardening and softening in binary iron alloys. J Mater Sci 1996;31:1087–99.
[81] Khater H, Monnet G, Terentyev D, Serra A. Dislocation glide in Fe–carbon solid solution: from atomistic to continuum level description. Int J Plast 2014;62:34–49.
[82] Dethloff C, Gaganidze E, Aktaa J. Review and critical assessment of dislocation loop analyses on eurofer 97. Nucl Mater Energy 2018;15:23–6.
[83] Byun T, Farrel K. Irradiation hardening behavior of polycrystalline metals after low temperature irradiation. J Nucl Mater 2004;326:86–96.
[84] Grossbeck M. 1.04 - Effect of radiation and strength and ductility of metals and alloys. Mater Sci Mater Eng 2012;1:99–122.
[85] Lucon E, Vanermeulen W. Overview of the tensile properties of EUROFER in the unirradiated and irradiated conditions. J Nucl Mater 2009;386–388:254–6.
[86] Zinovev A, Chang C-C, Van Eyken J, Gaganidze E, Terentyev D. Effect of neutron irradiation to 0.7 dpa and 1.4 dpa on the tensile properties and fracture surface of EUROFER97 steel. J Nucl Mater 2023;587:154742.
[87] Lin H, Shao L, Lv L, Bao J. Investigation of the evolution of plastic anisotropy and pile-up of Al single crystal in nanoindentation using different crystal plasticity models. J Mater Sci Technol 2024;65(5):494–501.
[88] Duerrschnabel M, Jäntsch U, Gaisin R, Rieth M. Microstructural insights into EUROFER97 batch 3 steels. Nucl Mater Energy 2023;35:101445.
[89] Fernández P, Lancha A, Lapeña J, Serrano M, Hernández-Mayoral M. Metallurgical properties of reduced activation martensitic steel Eurofer'97 in the as-received condition and after thermal ageing. J Nucl Mater 2002;307–311(Part 1):495–9.
[90] Hargreaves J, Tipping H, Moore S, Kumar D, Harding L, Dominguez Andrade H, Bell C, Hanna P, Dawson H, Martin T. The transient thermal ageing of Eurofer 97 by mitigated plasma disruptions. Mater Des 2024;244:113207.
[91] Das A, Altstadt E, Kaden C, Kapoor G, Akhmadaliev S, Bergner F. Nanoindentation response of ion-irradiated Fe, Fe-Cr alloys and ferritic-martensitic steel Eurofer 97: The effect of ion energy. Front Mater 2022;8.
[92] Kareer A, Prasitthipayong A, Krumwiede D, Collins D, Hosemann P, Roberts S. An analytical method to extract irradiation hardening from nanoindentation hardness-depth curves. J Nucl Mater 2018;498:274–81.
[93] Bergner F, Kaden C, Das A, Merino S, Diego G, Hähner P. Nanoindentation applied to ion-irradiated and neutron-irradiated Fe-9Cr and Fe-9Cr-NiSiP model alloys. J Appl Phys 2022;132:045101.
[94] Hosemann P, Kiener D, Wang Y, Maloy SA. Issues to consider using nano indentation on shallow ion beam irradiated materials. J Nucl Mater 2012;425(1–3):136–9.
[95] Kramer D, Huang H, Kriese M, Robach J, Nelson J, Wright A, Bahr D, W.W. G. Yield strength predictions from the plastic zone around nanocontacts. Acta Mater 1998;47(1):333–43.
[96] Mecking H. Work hardening of single-phase polycrystals. In: Encyclopedia of materials: Science and technology. 2nd ed.. Elsevier; 2001, p. 9785–94.
[97] Zinovev A, Delannay L, Terentyev D. Plastic deformation of ITER specification tungsten: Temperature and strain rate dependent constitutive law deduced by inverse finite element analysis. Int J Refract Met Hard Mater 2021;96:105481.
[98] Wu L, Zulueta K, Major Z, Arriaga A, Noels L. Bayesian inference of non-linear multiscale model parameters accelerated by a deep neural network. Comput Methods Appl Mech Engrg 2020;360:112693.